Journal of Sound and Vibration 326 (2009) 909–938

Contents lists available at ScienceDirect

Journal of Sound and Vibration

journal homepage: www.elsevier.com/locate/jsvi

Vibration mode shape recognition using image processing

Weizhuo Wang [a], John E Mottershead [a,*], Cristinel Mares [b]

[a] Department of Engineering, The University of Liverpool, Liverpool L69 3GH, UK
[b] School of Engineering and Design, Brunel University, Middlesex UB8 3PH, UK

ARTICLE INFO

Article history:
Received 19 January 2009
Received in revised form
20 April 2009
Accepted 12 May 2009
Handling Editor: K. Shin
Available online 21 June 2009

ABSTRACT

Currently the most widely used method for comparing mode shapes from finite elements and experimental measurements is the modal assurance criterion (MAC), which can be interpreted as the cosine of the angle between the numerical and measured eigenvectors. However, the eigenvectors only contain the displacement of discrete coordinates, so that the MAC index carries no explicit information on shape features. New techniques, based upon the well-developed philosophies of image processing (IP) and pattern recognition (PR) are considered in this paper. The Zernike moment descriptor (ZMD), Fourier descriptor (FD), and wavelet descriptor (WD) are the most popular shape descriptors due to their outstanding properties in IP and PR. These include (1) for the ZMD-rotational invariance, expression and computing efficiency, ease of reconstruction and robustness to noise; (2) for the FD—separation of the global shape and shape-details by low and high frequency components, respectively, invariance under geometric transformation; (3) for the WD—multi-scale representation and local feature detection. Once a shape descriptor has been adopted, the comparison of mode shapes is transformed to a comparison of multidimensional shape feature vectors. Deterministic and statistical methods are presented. The deterministic problem of measuring the degree of similarity between two mode shapes (possibly one from a vibration test and the other from a finite element model) may be carried out using Pearson's correlation. Similar shape feature vectors may be arranged in clusters separated by Euclidian distances in the feature space. In the statistical analysis we are typically concerned with the classification of a test mode shape according to clusters of shape feature vectors obtained from a randomised finite element model. The dimension of the statistical problem may often be reduced by principal component analysis. Then, in addition to the Euclidian distance, the Mahalanobis distance, defining the separation of the test point from the cluster in terms of its standard deviation, becomes an important measure. Bayesian decision theory may be applied to formally minimise the risk of misclassification of the test shape feature vector. In this paper the ZMD is applied to the problem of mode shape recognition for a circular plate. Results show that the ZMD has considerable advantages over the traditional MAC index when identifying the cyclically symmetric mode shapes that occur in axisymmetric structures at identical frequencies. Mode shape recognition of rectangular plates is carried out by the FD. Also, the WD is applied to the problem of recognising the mode shapes in the thin and thick regions of a plate with different thicknesses. It shows the benefit of using the WD to identify mode-shapes having both local and global components. The comparison and classification of mode shapes using IP and PR provides a 'toolkit' to complement the

* Corresponding author.
E-mail address: j.e.mottershead@liverpool.ac.uk

doi:10.1016/j.jsv.2009.05.024

conventional MAC approach. The selection of a particular shape descriptor and classification method will depend upon the problem in hand and the experience of the analyst.

1. Introduction

Validating and updating a mathematical model [1] by experimental results is a well-known strategy in design optimisation. In structural dynamics, comparing mode shapes between prediction and measurement is a crucial step. The current method, the *modal assurance criterion* (MAC) [2], works perfectly well with small and medium-sized structures. However, the MAC is inadequate to show the subtle difference between analytical and measured mode shapes especially since new computing and testing techniques have emerged. Modern computing power for detailed finite element models and advanced full-field optical measurement techniques such as the *scanning laser Doppler vibrometer* (SLDV) [3,4] and *digital image correlation* (DIC) [5] make accurate dynamic characteristics available for large and complicated structures. Well developed techniques in *image processing* (IP) and *pattern recognition* (PR) enable versatile comparison and classification of mode shapes [6–8]. Within such procedures, a series of shape features with good discriminative capability should be extracted to form a feature vector—*shape descriptor* (SD). Now the similarity/dissimilarity of the shapes can be revealed by the 'distance' of their corresponding SDs in the shape feature space according to appropriate criteria.

The moment descriptor is one of the most popular shape descriptors in IP and PR of two dimensional (2D) images and shape patterns [9,10]. Hu [11] first introduced a set of moment invariants constructed by non-linear combinations of *geometric moments* (GM). These geometric moment invariants have the properties of being invariant under image translation, scaling and rotation. However, the non-orthogonality of the moment basis leads to redundancy of information, making it is difficult to recover the original shape unambiguously from the shape descriptors.

Teague [12] suggested using orthogonal polynomials to replace the algebraic polynomials when calculating the moment descriptor. The *Zernike moment* (ZM) is based on a complete set of orthogonal polynomials over a circle of unit radius—Zernike polynomials. It was found later that the Zernike moment is one of the most important region-based shape descriptors because of its outstanding properties resulting from the orthogonality of the Zernike polynomials. Firstly, expressing an image as a set of mutually independent descriptors has the effect of minimising the redundancy of information. Secondly, the contribution of each order of moment to the image reconstruction can be separated, so that the process of regaining the original image is much easier than by geometric moment descriptors [13]. Rotational invariance [14,15] is another important property of the ZM, meaning that rotating an image does not change the magnitudes of its Zernike moments. Also, the ZM is robust to noise [13] and effective, so that a small number of Zernike moments are usually sufficient for shape reconstruction.

Fourier Descriptors (FDs) were originally proposed in 1960 by Cosgriff [16], and thereafter became popular among the pattern recognition community through the papers of Zahn [17], Granlund [18], and Fu [19]. FDs are among the most popular shape representation methods for vision and pattern recognition applications. FDs refer to a class of methods, not a single method, since there are many different ways in which the FDs of a shape can be defined. The basic idea underlying this approach consists in representing the shape of interest in terms of a 1D, 2D or even 3D signal. The Fourier transform of this signal is determined and the FDs are calculated for this Fourier representation. Some properties of the FDs directly follow from the underlying theory of the Fourier transforms and series. For instance, the 0th component of the FDs obtained from the contour representation is associated with the centroid of the original shape. The invariance to geometric transformations is also a direct consequence of the properties of the Fourier series. Such properties have helped to popularize this shape representation scheme, which has been adopted in a number of applications during the last four decades.

In certain applications, local shape information is especially significant, so that certain important shape features are associated with a particular portion of the object, such as a discontinuity, singularity or local frequency. *The short-time Fourier descriptor* (*SFD*) [20] and *wavelet descriptor* (*WD*) [21,22] are two of the most powerful methods for detecting these local shape features. One of the main properties of the wavelet descriptor is its ability to separate local features from the global shape. For example a partial occlusion may interfere significantly with a global Fourier descriptor or moment descriptor, while the wavelet descriptor is not affected at all.

The SDs may be assembled together in the *shape feature vector* (SFV). The comparison of mode shapes is then transformed to a similarity measurement between the SFVs in the feature space. Dimensionless normalisation for the SFV is necessary before commencing the comparison to avoid the scaling effect. For example, the SFV may be normalised by subtracting its mean value and then dividing by its standard deviation. The comparison of SFVs may be achieved by Pearson's correlation, which is similar to the MAC correlation except that it is carried out using the shape feature vector rather than the vector of coordinate displacements. The shape feature vector has the effect of concentrating the shape information into a small number of meaningful terms whereas there is generally much redundancy in the untreated vector of coordinate displacements. Clustering techniques are used to establish the similarity between different mode shapes. In hierarchical clustering, SFVs grouped together according to distance measures are shown as 'twigs' on the dendrogram. Twigs that are close to each other are considered to represent similar mode shapes.

When modes shapes are measured in the presence of uncertainty, then the comparison of SFVs becomes a stochastic problem. Statistical pattern recognition techniques provide a range of methods [7] for the classification of the SFVs. The basic idea of the statistical approach is to select suitable features that allow the SFVs of the shapes in the same class to be as compact as possible in the feature space; while SFVs of two shapes from distinct classes are as loose as possible. Bayesian decision theory [23], discriminant functions [24] and clustering [25] are frequently adopted.

In the next section, different shape descriptors are defined. The comparison of SFVs based on statistical methods is described in Section 3. The application of SDs for mode-shape recognition is illustrated using several simple structural examples in Section 4.

2. Shape descriptors

The SD of an image (mode shape) may be considered as a point in the shape-feature vector space. 2D mode shapes are considered in this paper. Thus, the general form of SD can be expressed as

$$\mathscr{D} = \mathscr{J}[I(x,y)] \tag{1}$$

where $I(x,y)$ denotes the continuous-displacement mode shape function and $\mathscr{J}[*]$ represents the transformation for extracting the shape features. More specifically, the SD can be defined by projecting the image function onto a kernel function $\Re(x,y)$ as

$$\mathscr{D} = \int_{\Omega} \Re(x,y) I(x,y)\,\mathrm{d}x\,\mathrm{d}y \tag{2}$$

where Ω denotes the domain of definition. Different types of SDs (ZMDs, FDs, WDs etc.) are defined by using different kernel functions.

2.1. Zernike moment descriptor

A set of 2D complex polynomials defined over a unit circle was introduced by Zernike [26],

$$V_{n,m}(x,y) \equiv V_{n,m}(\rho,\vartheta) = R_{n,m}(\rho)\mathrm{e}^{\mathrm{i}m\vartheta} \tag{3}$$

where $\mathrm{i} = \sqrt{-1}$, (ρ,ϑ) is the polar coordinate, n is the non-negative integer, representing the order of the radial polynomial; m is the positive and negative integers subject to constraints $n-|m|$ even, $|m| \le n$ representing the repetition of the azimuthal angle; $R_{n,m}$ is the radial polynomial,

$$R_{n,m}(\rho) = \sum_{s=0}^{(n-|m|)/2} (-1)^s \frac{(n-s)!}{s!\left(\frac{n+|m|}{2}-s\right)!\left(\frac{n-|m|}{2}-s\right)!}\rho^{n-2s} \tag{4}$$

According to the orthogonality properties [27], the inner product of any pair of complex Zernike polynomials can be expressed as

$$\int\int_{x^2+y^2\le 1} V_{p,q}(x,y)V^*_{n,m}(x,y)\mathrm{d}x\,\mathrm{d}y = \frac{\pi}{n+1}\delta_{n,p}\delta_{m,q} \tag{5}$$

where * denotes the complex conjugate and $\delta_{n,p}$ and $\delta_{m,q}$ are Kronecker deltas. Thus, the Zernike moment descriptor can be obtained by substituting the Zernike polynomials into the kernel function in (2) as

$$\mathscr{D}_{Z_{n,m}} = \frac{n+1}{\pi}\int\int_{x^2+y^2\le 1} I(x,y)V^*_{n,m}(x,y)\,\mathrm{d}x\,\mathrm{d}y \tag{6}$$

or, expressed in polar coordinates as

$$\mathscr{D}_{Z_{n,m}} = \frac{n+1}{\pi}\int_0^{2\pi}\int_0^1 I(\rho,\vartheta)V^*_{n,m}(\rho,\vartheta)\rho\,\mathrm{d}\rho\,\mathrm{d}\vartheta \tag{7}$$

Eqs. (6) and (7) show that the ZMDs are the inner products of the image and a series of orthogonal Zernike Polynomials. Thus, the original image $I(\rho,\vartheta)$ may easily be reconstructed by summing together all the products of the decomposition coefficients (ZMD) and their corresponding Zernike polynomials as [12],

$$I(\rho,\vartheta) = \sum_{n=0}^{\infty}\sum_{m}\mathscr{D}_{Z_{n,m}}V_{n,m}(\rho,\vartheta) \tag{8}$$

where m is constrained as in Eq. (3). Expression efficiency is one of the important properties of the ZMD, meaning the main shape information may be extracted by the lower order moments after truncating the higher orders of the ZMD in real applications. Therefore, the finitely reconstructed image $\hat{I}(\rho,\vartheta)$ obtained by keeping the moments from order 0 to N_{max} and

discarding the remaining higher order Zernike polynomials may be written as

$$\hat{I}(\rho,\vartheta)=\sum_{n=0}^{N_{max}}\sum_{m}\mathscr{D}_{Z_{n,m}}V_{n,m}(\rho,\vartheta) \tag{9}$$

The sufficient number N_{max} to be retained may be determined by comparing the similarity between the original image and the reconstructed image by the ZMDs up to N_{max}. Such comparisons may be carried out using the correlation coefficient,

$$\varrho(\hat{I},I)=\frac{\int\int_{\Omega}(\hat{I}-\bar{\hat{I}})(I-\bar{I})\,\mathrm{d}A}{\sqrt{[\int\int_{\Omega}(\hat{I}-\bar{\hat{I}})^2\mathrm{d}A][\int\int_{\Omega}(I-\bar{I})^2\mathrm{d}A]}} \tag{10}$$

where Ω denotes the internal domain of the unit disc, dA is the infinitesimal area, and

$$\bar{\hat{I}}=\frac{\int\int_{\Omega}\hat{I}\mathrm{d}A}{\int\int_{\Omega}\mathrm{d}A} \tag{11}$$

$$\bar{I}=\frac{\int\int_{\Omega}I\mathrm{d}A}{\int\int_{\Omega}\mathrm{d}A} \tag{12}$$

Rotational invariance is another significant property [15] of the ZMD. Suppose the image $I(\rho,\vartheta)$ is rotated through an angle α with respect to the z-axis,

$$I^{r}(\rho,\vartheta)=I(\rho,\vartheta-\alpha) \tag{13}$$

The relation between their ZMDs can be expressed as

$$|\mathscr{D}_{Z^{r}_{n,m}}|=|\mathscr{D}_{Z_{n,m}}| \tag{14}$$

and

$$\arg(\mathscr{D}_{Z^{r}_{n,m}})=\arg(\mathscr{D}_{Z_{n,m}})-m\alpha \tag{15}$$

These properties are very useful for recognising mode shapes of axisymmetric structures, as will be demonstrated in Section 4.

2.2. Fourier descriptor

The FD is based on the frequency components of the *Fourier transform* (FT) applied to the image. According to the well-known theory of the FT, the kernel function of the SD should be the complex valued sinusoid,

$$\mathscr{D}_{\mathscr{F}}(u,v)=\int_{-\infty}^{+\infty}\int_{-\infty}^{+\infty}\mathrm{e}^{-\mathrm{i}2\pi(ux+uy)}I(x,y)\,\mathrm{d}x\,\mathrm{d}y \tag{16}$$

$\mathscr{D}_{\mathscr{F}}(u,v)$ is a continuous function having the same cardinality as $I(x,y)$ and for real applications, this should to be reduced whilst retaining as much information as possible. It is noted that only the low frequency and higher energy components are sufficient to describe the shape. For instance, elliptical descriptors (with *centroid*, *orientation*, *eccentricity* and *spread* described on page 422 of [8]) based on the FD spectrum are feasible to indicate the distribution of the frequency energy. Also, the FD spectrum can be divided into non-overlapping sub-bands. The average energy from each sub-band then becomes an element of the feature vector. The latter extraction method is easily implemented when applying the *discrete Fourier transform* (DFT),

$$\mathscr{D}_{\mathscr{F}}(u,v)=\frac{1}{KL}\sum_{k=0}^{K-1}\sum_{\ell=0}^{L-1}\mathrm{e}^{-\mathrm{i}2\pi((uk/K)+(v\ell/L))}I(k,\ell) \tag{17}$$

We considered the recognition of real valued mode shapes (normal modes). According to the properties of the FT, $\mathscr{D}_{\mathscr{F}}(u,v)$ is symmetric under conjugation, $\mathscr{D}_{\mathscr{F}}(u,v)=\mathscr{D}^{*}_{\mathscr{F}}(-u,-v)$. In additional, some of the mode shapes are axisymmetric, $I(x,y)=I(x,-y)$ or anti-axisymmetric, $I(x,y)=-I(x,-y)$. Their corresponding FDs can be expressed as $\mathscr{D}_{\mathscr{F}}(u,v)=-\mathscr{D}_{\mathscr{F}}(u,-v)$ and $\mathscr{D}_{\mathscr{F}}(u,v)=\mathscr{D}_{\mathscr{F}}(u,-v)$ respectively. These symmetric properties indicate that the mode shapes can be uniquely determined by only the non-negative components in the spatial frequency plane. Thus, the dimensionality of the SFV formed by the FDs , $\mathbf{f}_{FD}$, can be further reduced.

Reconstruction is straight forward by applying the inverse Fourier transform. Good approximation may be obtained by retaining a sufficient number of higher energy terms. The same criterion as in Eq. (10) may be used to determine the necessary dimensionality of the SFV.

2.3. Wavelet descriptor

The idea of wavelet transformation is to represent an image in terms of the superposition of wavelets with different scale levels and positions. The wavelet, having better time-frequency resolution than the *short-time Fourier transform* (STFT) [28], may be expressed as

$$\psi_{b_x,b_y,a} = \frac{1}{a}\psi\left(\frac{x-b_x}{a}, \frac{y-b_y}{a}\right) \tag{18}$$

where $a \in \mathbb{R}^+$ is the dilating scale parameter, $(b_x, b_y) \in \mathbb{R}^2$ are the translation parameters and $\psi_{b_x,b_y,a}$ is the translated and dilated version of the mother wavelet $\psi(x,y)$. The normalisation factor $1/a$ is included so that $\|\psi_{b_x,b_y,a}\| = \|\psi\|$. Depending on the application, these parameters take either continuous or discrete values. The definition of *continuous wavelet transform* (CWT) can be expressed as an inner product of the wavelet and the image,

$$\begin{aligned}\mathscr{D}_{\mathscr{W}}(a, b_x, b_y) &= \langle \psi_{b_x,b_y,a}, I(x,y)\rangle \\ &= \int_{-\infty}^{+\infty}\int_{-\infty}^{+\infty} \psi^*_{b_x,b_y,a}(x,y) I(x,y)\,\mathrm{d}x\,\mathrm{d}y\end{aligned} \tag{19}$$

The mother wavelet must satisfy

$$\int_{-\infty}^{+\infty}\int_{-\infty}^{+\infty} \psi(x,y)\,\mathrm{d}x\,\mathrm{d}y = 0 \tag{20}$$

so that the wavelet is oscillatory with a null DC component.

Discretization of the wavelet parameters is adopted in many applications [28]. The most common choice in practise is obtained by letting $a = 2^{-s}$, $b_x = 2^{-s}k$, $b_y = 2^{-s}\ell$ with $s, k, \ell \in \mathbb{Z}$ (integers). This results in the *discrete wavelet transform* (DWT).

A number of orthonormal wavelet bases may be constructed [29]. In image processing the great power of the DWT in lies in its application to *multiresolution analysis* (MRA) [21]. A one dimensional (1D) signal $f(x)$, may be approximated by using a hierarchical framework with different resolutions. Two related functions, the mother wavelet function ψ and the scaling function ϕ, are introduced with their dyadic dilated and translated in integer steps, $\psi_{s,n}(x) = \sqrt{2^s}\psi(2^s x - n)$ and $\phi_{s,n}(x) = \sqrt{2^s}\phi(2^s x - n)$, $s, n \in \mathbb{Z}$. For any fixed s, the scaling functions $\phi_{s,n}$ are constructed to be orthonormal. The subspaces $\boldsymbol{A}_s$ spanned by $\phi_{s,n}$ describe the successive approximation spaces, $\{0\} \subset \cdots \boldsymbol{A}_{-2} \subset \boldsymbol{A}_{-1} \subset \boldsymbol{A}_0 \subset \boldsymbol{A}_1 \subset \boldsymbol{A}_2 \cdots \subset L^2(\mathbb{R})$, with respect to integer scales. When the signal is approximated by the coarser resolution 2^s, rather than the finer resolution 2^{s+1}, the loss of information is described by the wavelets at resolution 2^s. Thus, a subspace $\boldsymbol{W}_s$ spanned by the wavelet sequence $\psi_{s,n}$ complements the approximation space $\boldsymbol{A}_s$ in $\boldsymbol{A}_{s+1}$ orthogonally, so that $\boldsymbol{W}_s \perp \boldsymbol{A}_s$ and

$$\boldsymbol{A}_{s+1} = \boldsymbol{W}_s + \boldsymbol{A}_s \tag{21}$$

$$= \boldsymbol{W}_s + \boldsymbol{W}_{s-1} + \boldsymbol{A}_{s-1} \tag{22}$$

$$= \sum_{j=0}^{J-1} \boldsymbol{W}_{s-j} + \boldsymbol{A}_{s-J} \tag{23}$$

where J is the number of decomposition levels. In real applications, the signals obtained are usually sampled. Thus, a discrete signal may be considered as the initial approximation and be represented as an approximation by the scaling functions plus the details held by the wavelet functions at one step coarser resolution. The resulting approximation can be decomposed further by using the same procedure at successively coarser resolutions. Therefore, the input signal is characterised by the coefficients of the wavelets and scaling functions. These coefficients are determined as [21],

$$a_{j-1,n} = \sum_k h_{2n-k} a_{j,k} \tag{24}$$

and

$$w_{j-1,n} = \sum_k g_{2n-k} a_{j,k} \tag{25}$$

where $a_{s,n} = \langle f(x), \phi_{s,n}\rangle$, $w_{s,n} = \langle f(x), \psi_{s,n}\rangle$, $g_k = (-1)^k h_{1-k}$ and $h_n = \sqrt{2}\int \phi(x-n)\phi(2x)\,\mathrm{d}x$. Thus, the coefficients in different scales may be used as the components of SFV. For example, if we are interesting in the details of certain level, the SFV might be defined as $\mathrm{f}_s^w = \{w_{s,k}\}$.

The DWT may be extended to 2D images. Similar to the 1D case, scaling functions at approximation subspace $\boldsymbol{A}_s$ with resolution 2^s may be defined as [21],

$$\boldsymbol{\phi}_{s,k,\ell}(x,y) = \phi_{s,k}(x)\phi_{s,\ell}(y), \quad s, k, \ell \in \mathbb{Z} \tag{26}$$

where $\phi(\cdot)$ is the 1D scaling function, s is the scale and (k,ℓ) is the translation coordinate. The orthogonal complement subspace $\boldsymbol{W}_s$ of $\boldsymbol{A}_s$ in $\boldsymbol{A}_{s+1}$ can be built by three sets of wavelets which can be defined by associating the 1D wavelet $\psi(\cdot)$ and scaling functions $\phi(\cdot)$ as,

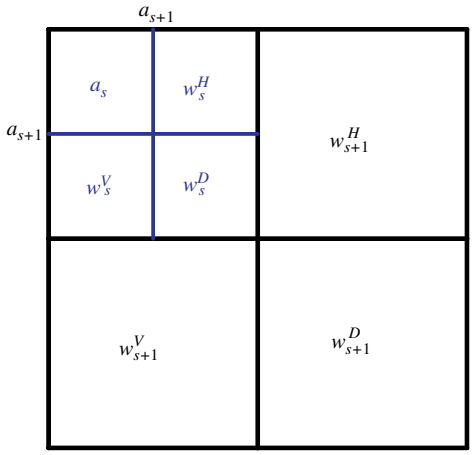

Fig. 1. Decomposition of sub-images between two scales.

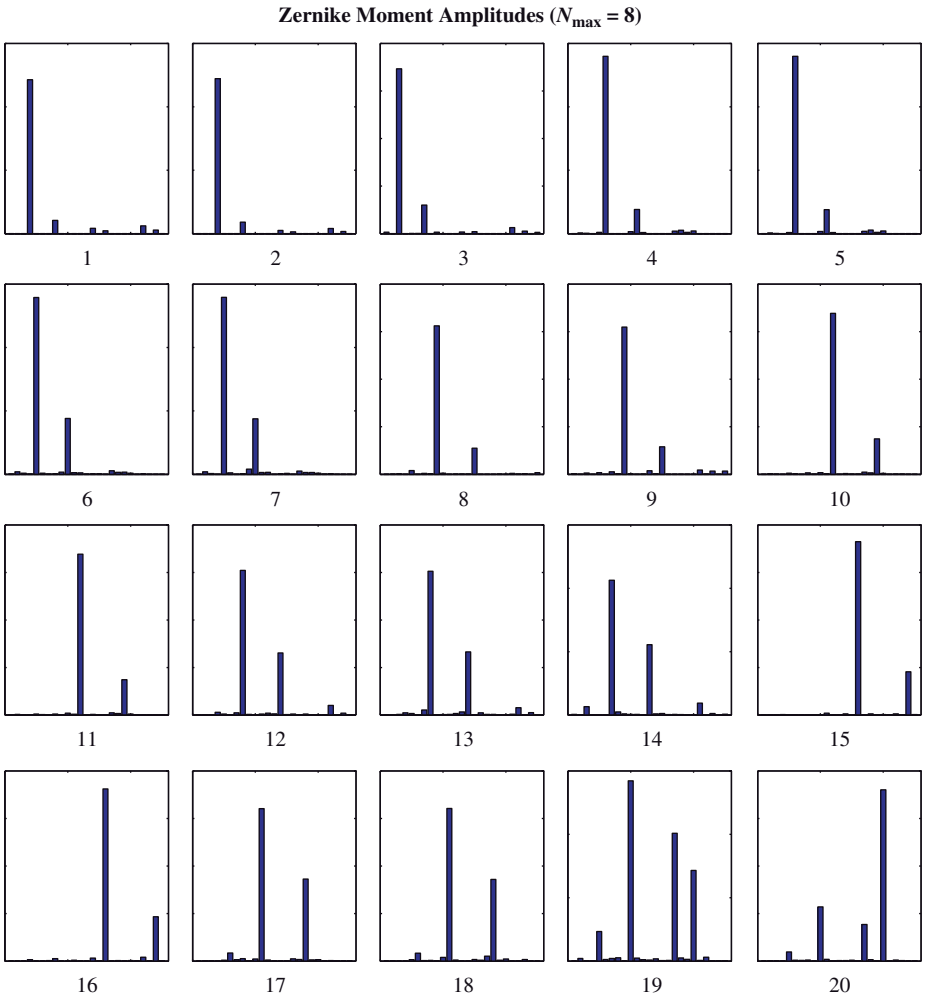

Fig. 2. Amplitudes of the ZMDs.

$$\text{Horizontal wavelets} \quad \psi^{H}_{s,k,\ell}(x,y) = \phi_{s,k}(x)\psi_{s,\ell}(y) \tag{27}$$

$$\text{Vertical wavelets} \quad \psi^{V}_{s,k,\ell}(x,y) = \psi_{s,k}(x)\phi_{s,\ell}(y) \tag{28}$$

$$\text{Diagonal wavelets} \quad \psi^{D}_{s,k,\ell}(x,y) = \psi_{s,k}(x)\psi_{s,\ell}(y) \tag{29}$$

which satisfy the admissibility condition (20).

Thus, the 2*D discrete wavelet transform* (DWT2) for an image can be obtained by implementing the 1D algorithm horizontally and then vertically. The outputs from each step of decomposition are the sub-images of one approximation at coarser resolution and three sub-images of detail in horizontal, vertical and diagonal directions as illustrated in Fig. 1. Thus, the comparison between images can now be carried out using the sub-images at different resolutions. The average energy of each sub-image may be used to form the SFV,

$$\mathbf{v}^{\text{dwt}} = \{v_{-J}, v^{H}_{-J}, v^{V}_{-J}, v^{D}_{-J}, v^{H}_{-J+1}, v^{V}_{-J+1}, v^{D}_{-J+1}, \ldots, v^{H}_{-1}, v^{V}_{-1}, v^{D}_{-1}\}^{\mathrm{T}} \tag{30}$$

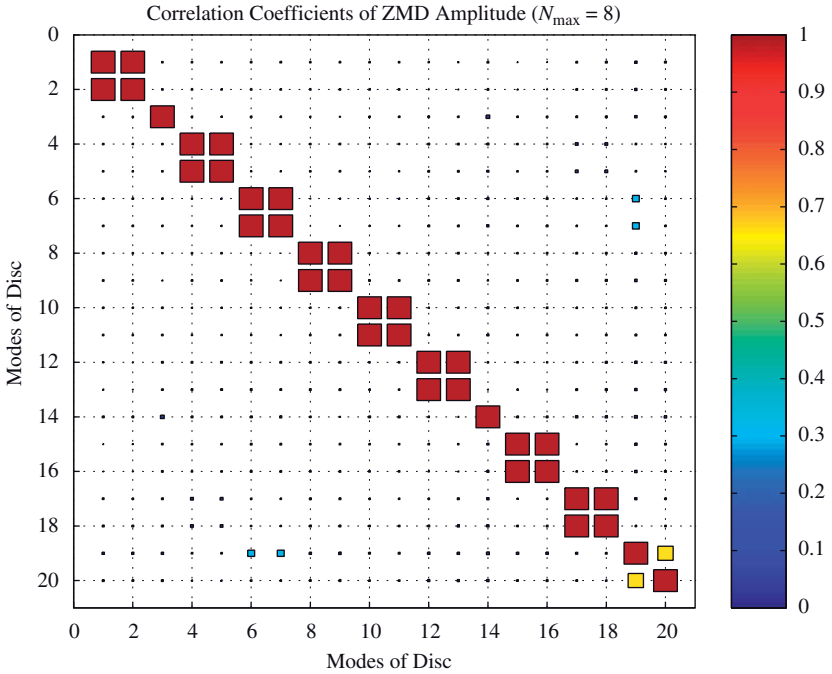

Fig. 3. Correlation coefficients of the ZMD amplitude.

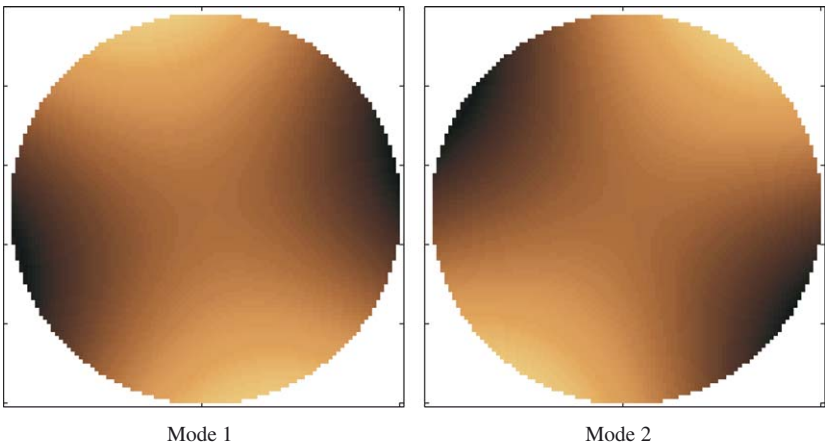

Fig. 4. Mode-shape patterns of modes 1 and 2.

where

$$v_{-J} = \frac{1}{K_{-J}L_{-J}} \sum_{k,\ell}^{K_{-J},L_{-J}} (a_{-J,k,\ell})^2 \tag{31}$$

is the average energy of the coarsest approximation coefficients defined by

$$a_{-J,k,\ell} = \langle I(x,y), 2^{-J}\phi(2^{-J}x-k, 2^{-J}y-\ell)\rangle \tag{32}$$

and

$$v_j^i = \frac{1}{K_j L_j} \sum_{k,\ell}^{k_j,L_j} (w_{j,k,\ell}^i)^2, \quad j=-J,-J+1,\ldots,-1, \quad i=H,V,D \tag{33}$$

where $(K_j \times L_j)$ is the size of the sub-image, J is the number of decompositions and $w_{j,k,\ell}^i$ is the wavelet coefficients at (k,ℓ) for the jth resolution defined as

$$w_{j,k,\ell}^i = \langle I(x,y), \psi_{s,k,\ell}^i\rangle \tag{34}$$

3. Statistical methods for SFV comparison

Shapes to be compared by statistical approaches are represented as l-dimensional feature vectors in the shape feature space. The intention is to select suitable features that allow the l-dimensional vectors of the shapes in the same class to be as compact as possible in the feature space; while feature vectors of two shapes from distinct classes are as loose as possible. Given a set of training shapes from each class, the objective is to establish decision boundaries in the feature space which separate shapes belonging to different classes. In the statistical decision theoretic approach, the decision boundaries are determined by the probability distributions of the patterns belonging to each class, which must either be specified or learned, for example, by a Bayesian classifier [23,30]. Another method is to define a set of boundaries that divide the feature space into different regions which correspond to each class, such as linear discriminant analysis, quadratic classifiers, etc. Clustering analysis is a powerful approach in unsupervised classification. This technique partitions the shapes into different clusters or groups. The term *unsupervised* means that the class labelling of the training shape patterns is not available. Therefore, the main objective of clustering analysis is to classify all the shapes into sensible clusters, which can be used to disclose the similarities and differences between the shapes and to draw meaningful conclusions from them. In this paper, correlation, *principal component analysis* (PCA), Bayesian decision theory and clustering techniques [25] are applied. A brief discussion of PCA and Bayesian classification may be found in Appendices A and B.

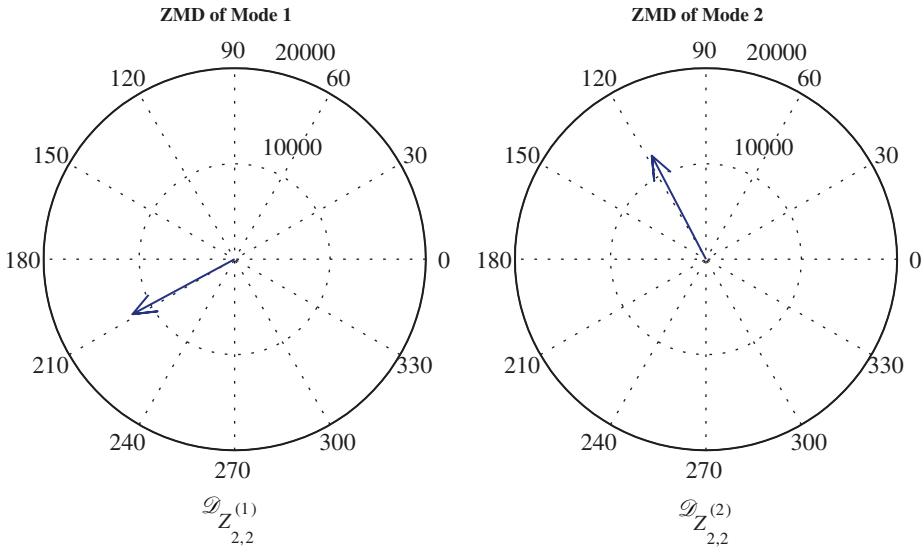

Fig. 5. Angular difference of modes 1 and 2 from $\mathscr{D}_{Z_{2,2}}$.

4. Examples

In this section, four cases based on different SDs are considered. The ZMD is applied to the problem of free vibration of a circular plate. Not only can the double modes of axisymmetric structures be revealed by the amplitudes of the ZMD but also their angular difference can be determined by phase information from the ZMD. The mode shapes of two rectangular thin plates, one stiffened by crossed ribs are compared by using a small number of high-energy FDs. Similar modal patterns of a plate are revealed using elliptical descriptors derived from the FDs. Local and global mode shape recognition is carried out using the WD for four rectangular plates with different thickness regions. Statistical classification methods are applied to the problem of a beam with uncertain boundary conditions.

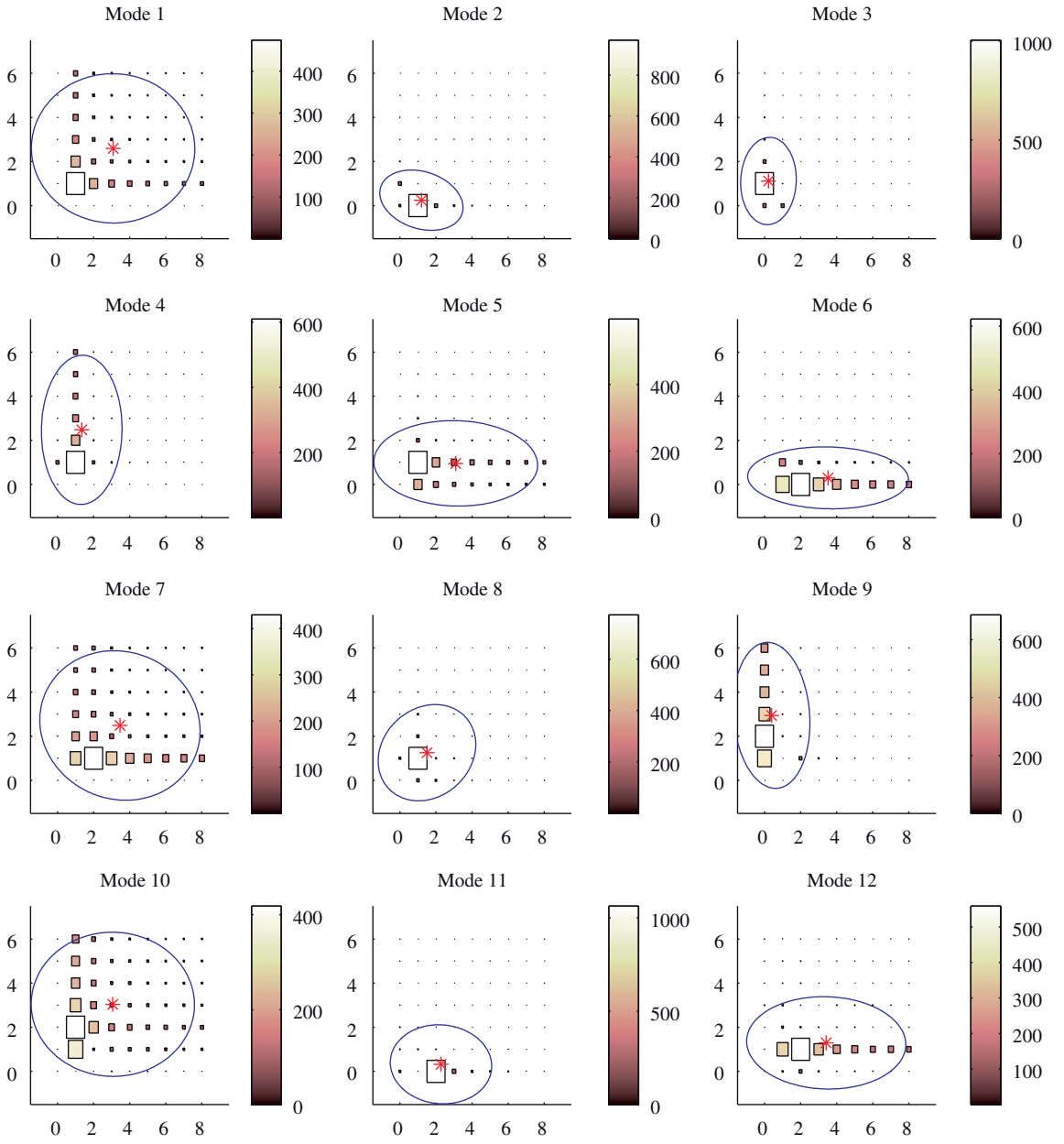

Fig. 6. Non-negative FD amplitudes and elliptical descriptors of modes 1–12.

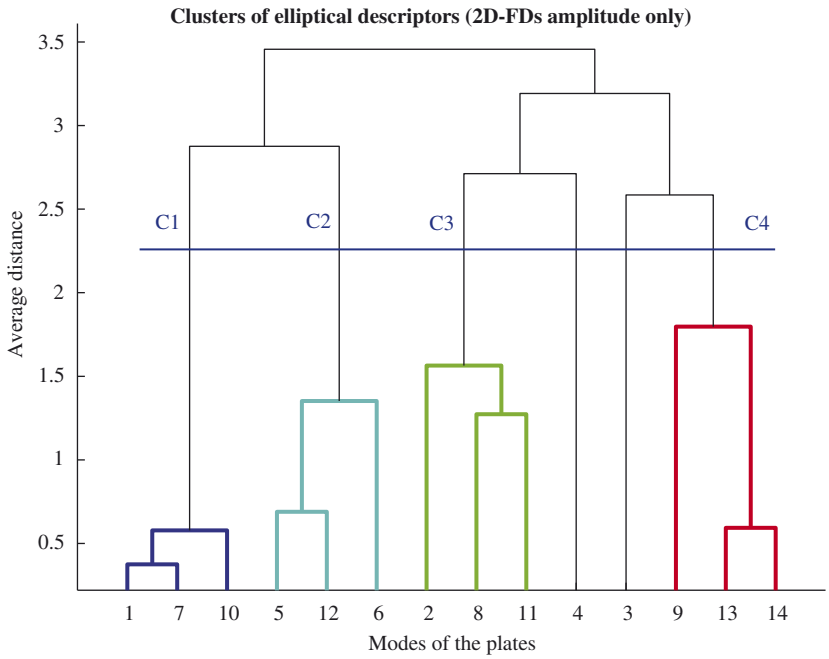

Fig. 7. Dendrogram by elliptical descriptor.

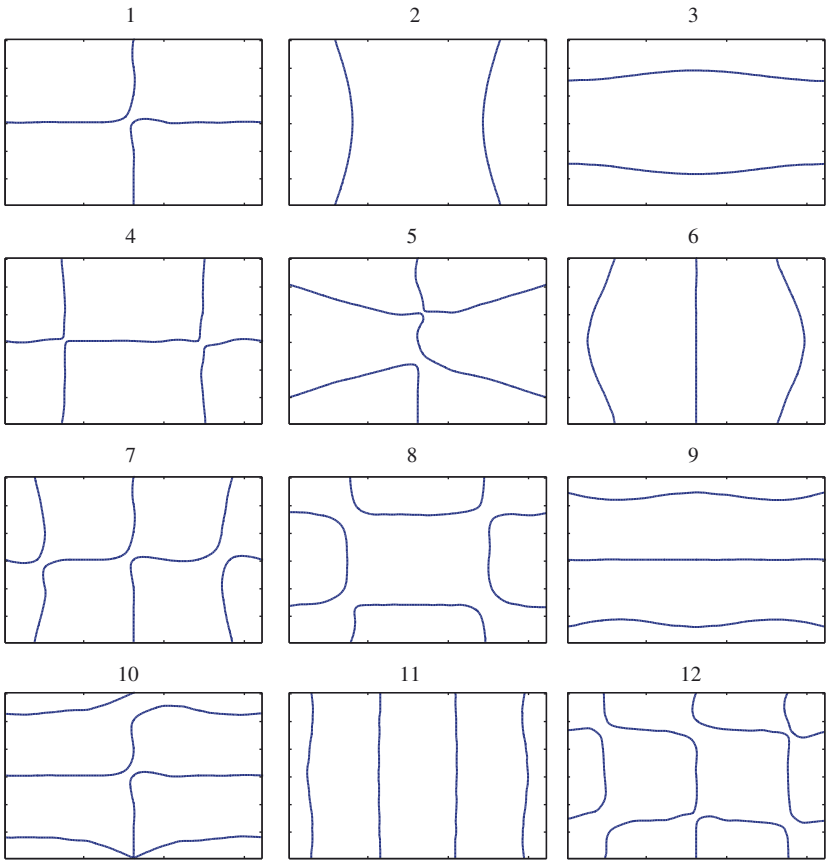

Fig. 8. Nodal lines of the rectangular plate.

4.1. ZMD of a circular plate

The free vibration of a circular plate is modelled by finite elements. Since the circular plate is a perfectly axisymmetric structure double modes are obtained. The conventional mode-shape comparison method, MAC, shows nothing about the double modes. Thus, the ZMD is applied to the first 20 modes. As illustrated in Fig. 2, the amplitudes of the Zernike moments from order 0 to 8 are shown in the figure. There are totally 25 Zernike moment amplitudes shown along the horizontal axis for each mode (subfigure). This overall number of the Zernike moments was determined by the indices $\{n, m\} = \{(0,0), (1,1), (2,0), (2,2), (3,1), (3,3), \ldots, (8,8)\}$ as defined in Eq. (3). It can also be seen that only a small number of the lower order ZMDs are needed to represent all the modes. This shows the ZMD to be an expression-efficient SD. The Pearson correlation coefficient [31] for mode shapes based on ZMD amplitudes is shown in Fig. 3 where the double modes can clearly be recognised.

The rotational difference between any pair of double modes can be determined by the ZMD property (15). The first pair of double modes 1 and 2 is shown in Fig. 4. As seen from Fig. 2 their ZMDs are mainly dominated by $\mathscr{D}_{Z_{2,2}}$. Thus, the angle

$$\alpha = \frac{(\arg(\mathscr{D}_{Z^{(2)}_{2,2}} - \arg(\mathscr{D}_{Z^{(1)}_{2,2}}))}{2} = \frac{90.1^\circ}{2} = 45.1^\circ$$

matches the theoretical angular difference between double modes 1 and 2 as in Fig. 5.

Further applications of the ZMD are discussed by the present authors [32], including the extension to non-circular structures, point-mass detection in a circular plate and finite element model updating.

4.2. FD of a rectangular plate

Free vibration of a $160 \times 120 \times 2$ mm rectangular aluminium thin plate is modelled. The FDs of the mode shapes are determined by the DFT. Since the structure is symmetric about the *x-axis* and about the *y-axis*, only the non-negative spatial frequency components need to be considered. Fig. 6 shows the amplitudes of the FDs for the first 12 modes in the first quadrant. The horizontal and vertical axes represent the spatial frequency coordinates u and v, respectively, as defined in Eq. (17). The size of the square represents the magnitude of the corresponding FD. It is noted that only a few lower

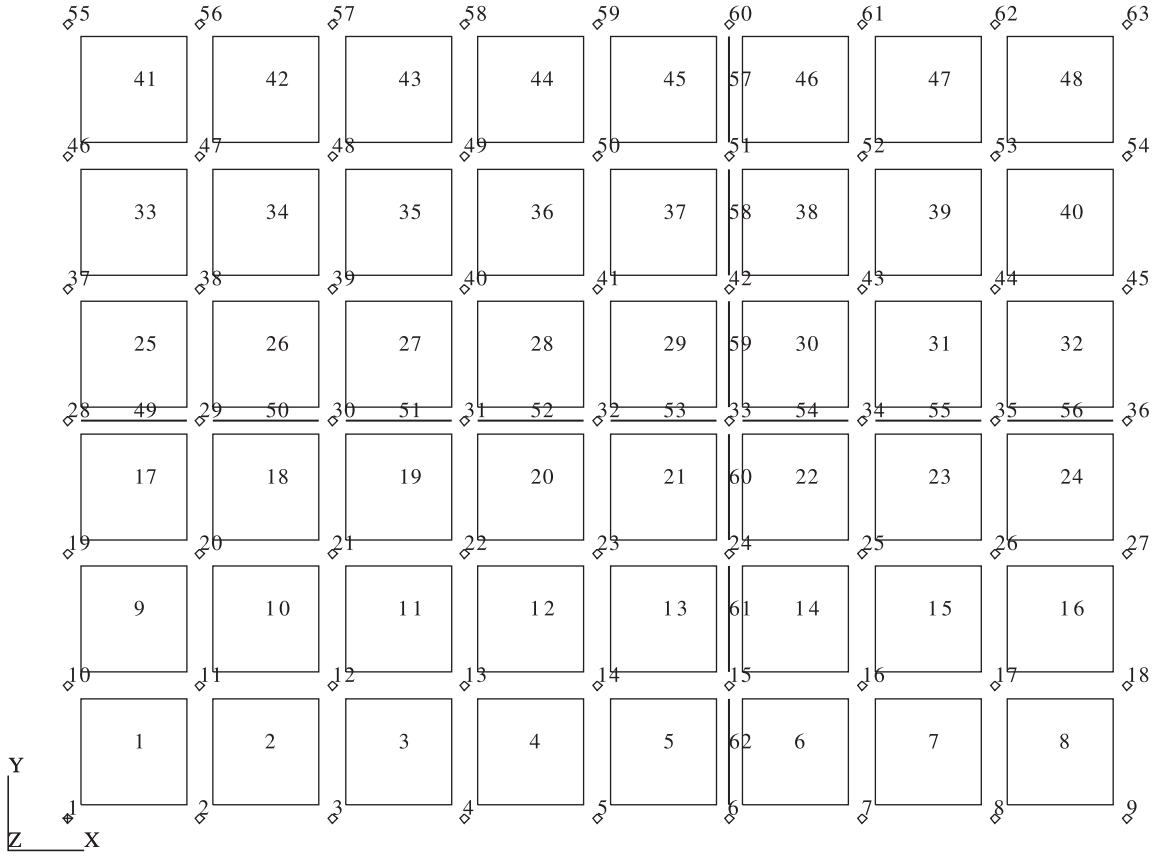

Fig. 9. FE model of the plate with ribs. The squares 1–48 are the quadrilateral plate elements and the bold line segments 49–62 are beam elements (ribs).

frequency components are significant. Higher level information is provided by elliptical descriptors, which describe the global spectrum pattern, also presented in the figures. It would be possible to apply Pearson's correlation, as in the previous ZMD example, using either the vector of FD terms directly or using the vector of elliptical descriptors. In this example it is chosen to apply a hierarchical clustering algorithm using elliptical descriptors from the FD spectrum and providing quantitative (average distance) measures between clusters of modes. Several clusters may be obtained by cutting the dendrogram [25] shown in Fig. 7 at a chosen distance separating the various groups of modes. The most compact cluster ***C1*** ((1,7),10) indicates the similarity of the three spectrum patterns as shown in Fig. 6. Cluster ***C2*** ((5,12),6) groups together those modes with a strongly dominant horizontal major axis of the ellipse. Also, the three compact ellipses having horizontal major axes are grouped by cluster ***C3*** (2,(8,11)). Furthermore, the similarities between FD patterns indicated by

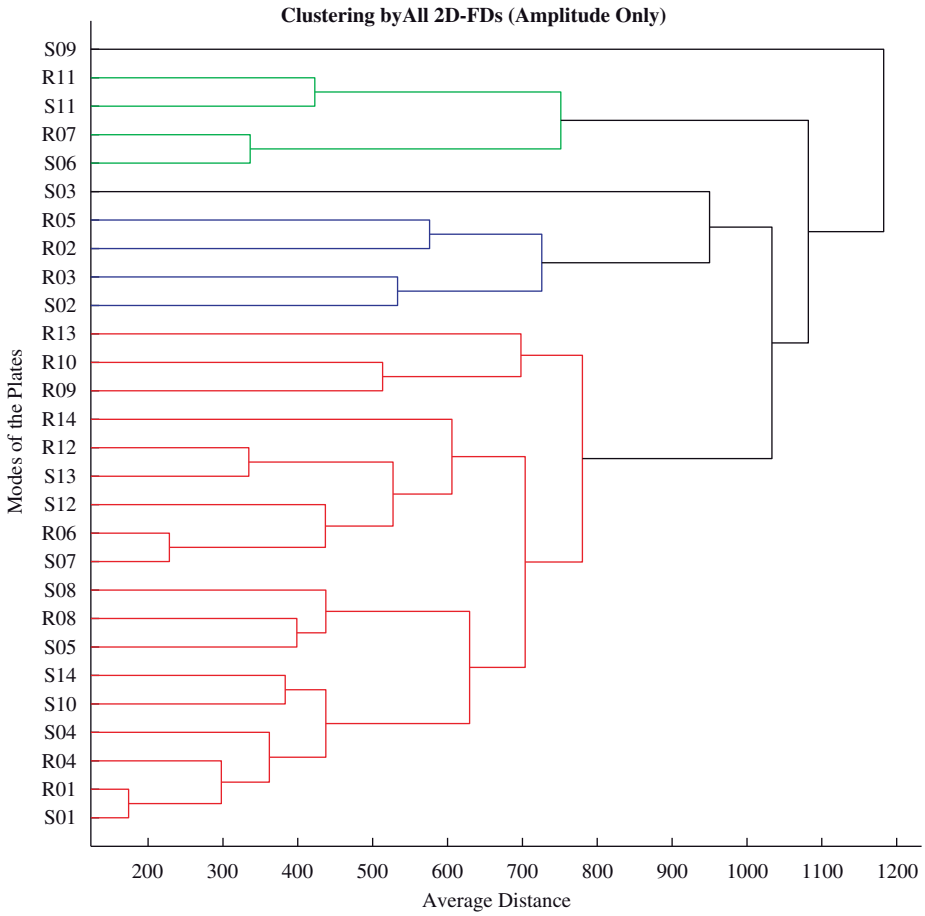

Fig. 10. Clustering by FDs for the simple and ribbed plates.

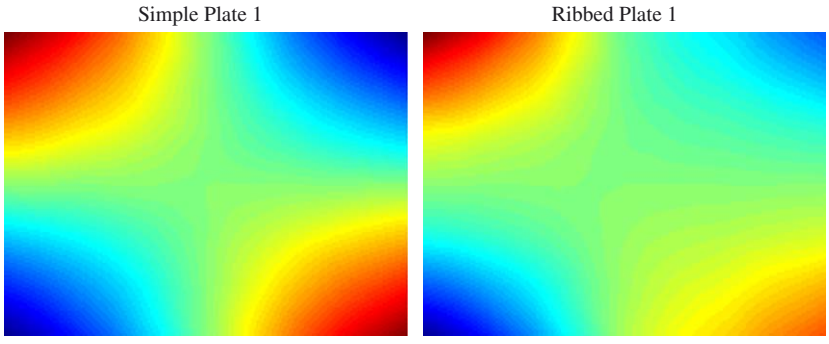

Fig. 11. Similar mode shape pairs S01 and R01.

these clusters can be referred back to the similarities between mode shapes. The nodal lines of the 12 modes are shown in Fig. 8. According to the closeness of modes 1, 7 and 10 (indicated by cluster ***C1***) it can be seen from their nodal lines that mode 7 has two more horizontal oscillations than mode 1 whilst mode 10 has two more vertical oscillations than mode 1. For cluster ***C2***, mode 12 has two more oscillations than mode 6 horizontally and mode 5 vertically. Similar relations between mode 2, 8 and 11 are indicated for cluster ***C3***. Thus the SFV formed by the elliptical descriptor of the FD spectrum

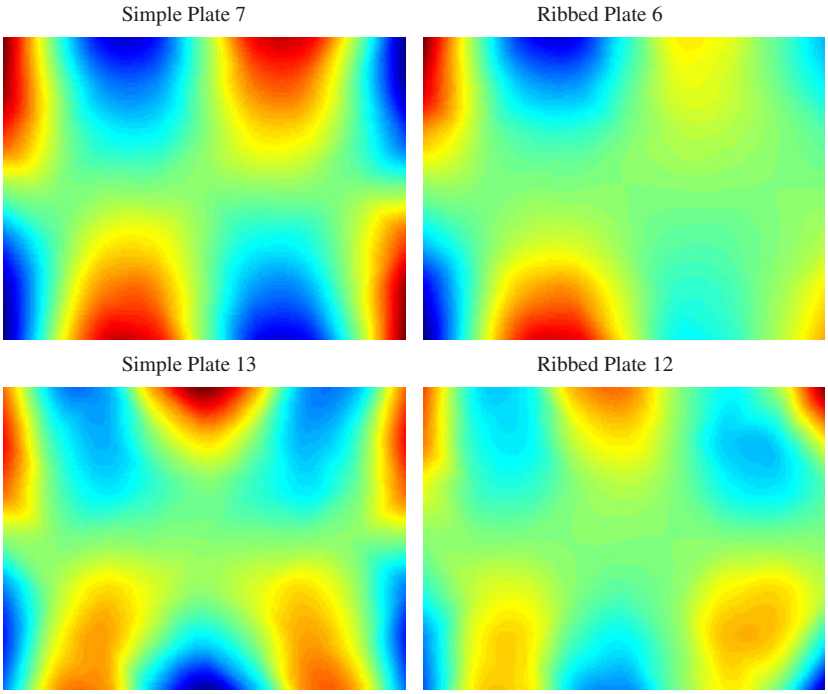

Fig. 12. Similar mode shape pairs S07 and R06, S13 and R12.

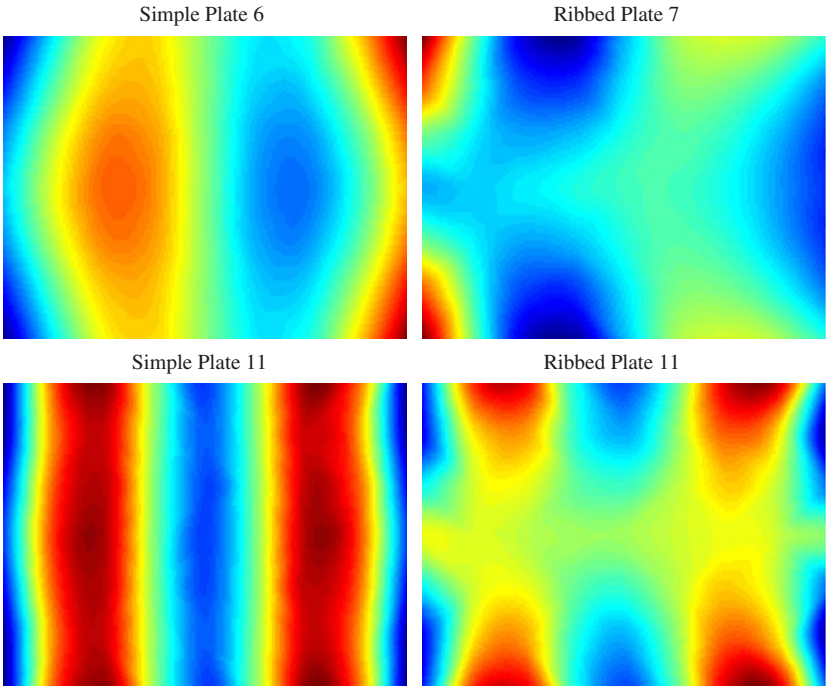

Fig. 13. Similar mode shape pairs S06 and R07, S11 and R11.

demonstrates the capability of discriminating between the various mode-shapes correctly and efficiently (the dimensionality of this SFV is 5).

Additionally, in order to obtain a more accurate comparison, the SFV may be based on the individual FDs sorted in descending magnitude order of their energies. In this case, the SFV is more powerful when recognising the mode shapes between two similar structures. e.g. with slightly different boundary conditions.

As shown in Fig. 9, the simple plate of the previous example is stiffened by two ribs. The mode-shape FDs were determined in the same way as for the simple plate. The similarity of mode shapes between the simple and ribbed plates via the hierarchical clustering of the Fourier descriptors is shown in Fig. 10. In this case, all the non-negative frequency FD components are considered. Similar mode shape pairs are clustered together in the dendrogram. For instance, the nearest pair is R01 and S01 where R denotes the ribbed plate; S denotes the simple plate and the following digits denote the modes. Other similar pairs such as R07 and S06, R11 and S11, R06 and S07, R12 and S13 etc. are gathered into clusters and their mode shape patterns are shown in Figs. 11–13 which demonstrates the similarities.

As mentioned before, only a small number of low frequency FDs are significant. Discarding the higher frequency and low energy components is feasible to reduce the dimensionality of the Fourier feature vector. The number of higher frequency and low energy FDs that might be neglected may be determined from the closeness of the reconstructed mode shape patterns with and without those FDs. In this case, the complete feature vectors $\mathbf{f}_{FD}$ including all non-negative frequency components of each mode for both plates are summarized to produce an overall FD energy vector. Here the term *energy* denotes the squared amplitude of the FDs. This energy vector is then sorted in descending order as shown in Fig. 14(a). The slope of the descending curve is steep from number 1 to 13 and flat for the remaining orders. Therefore, a sufficient and efficient Fourier feature vector $\mathbf{f}'_{FD}$ can be constructed by truncating the low energy components after number 13. The remaining FDs, after truncation (20 percent of the overall number) are shown in Fig. 14(b). As we can see that the most significant FD for all modes is the component with $u = 1$ and $v = 1$; the second is the one with $u = 2$ and $v = 1$ etc. The clustering of mode shapes based on these truncated Fourier feature vectors are almost identical to those created by the complete FDs. Also, the reconstructed shape patterns by the truncated Fourier feature vector $\mathbf{f}'_{FD}$ are very similar to the original shapes. Therefore, $\mathbf{f}'_{FD}$ is an appropriate shape feature vector for mode shape recognition of plate structures.

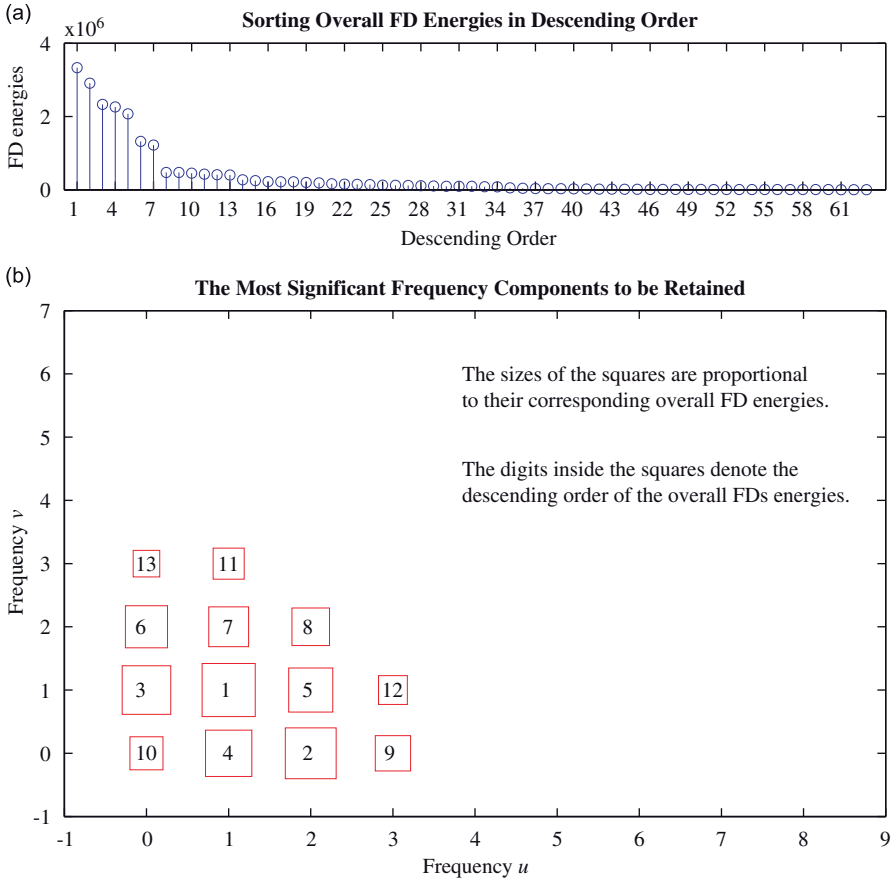

Fig. 14. Sorting the FD energies and retaining the 12 most significant frequency components.

Furthermore, it provides an adequate and computationally economic mode-shape indicator for correlation and updating of FE models.

4.3. WD of a rectangular plate with a thin region

Four rectangular plates with different thicknesses were modelled as shown in Fig. 15. The plates of Fig. 15(a) and (b) denoted by *pC* and *pCr* have two regions with different thickness. *pCr* has 'rims' at the edges of the thin region as shown in the figure. Another plate (*pN*) having the same size as the thin region of *pC* is shown in Fig. 15(c). The upper and left edges of *pN* are clamped whilst the others are free. The plate denoted by *pK* as shown in Fig. 15(d) has uniform thickness, the same as the thick region of *pCr*. Also, *pK* and *pCr* have the same height and width. The objectives of this section are to identify the thin region of the plate *pC* by the WD applied to the mode shapes and to recognise similar global mode shape patterns in plates *pCr* and *pK*.

Four levels of decomposition by the *rbio3.1* wavelet [28], shown in Fig. 16, were carried out on the mode shapes of the four plates. For each decomposition level, as in Fig. 1, there are four sub-images. i.e. one approximation at current level and three detail sub-images [21]. Thus, 13 sub-images were obtained for every single mode-shape four horizontal, four vertical,

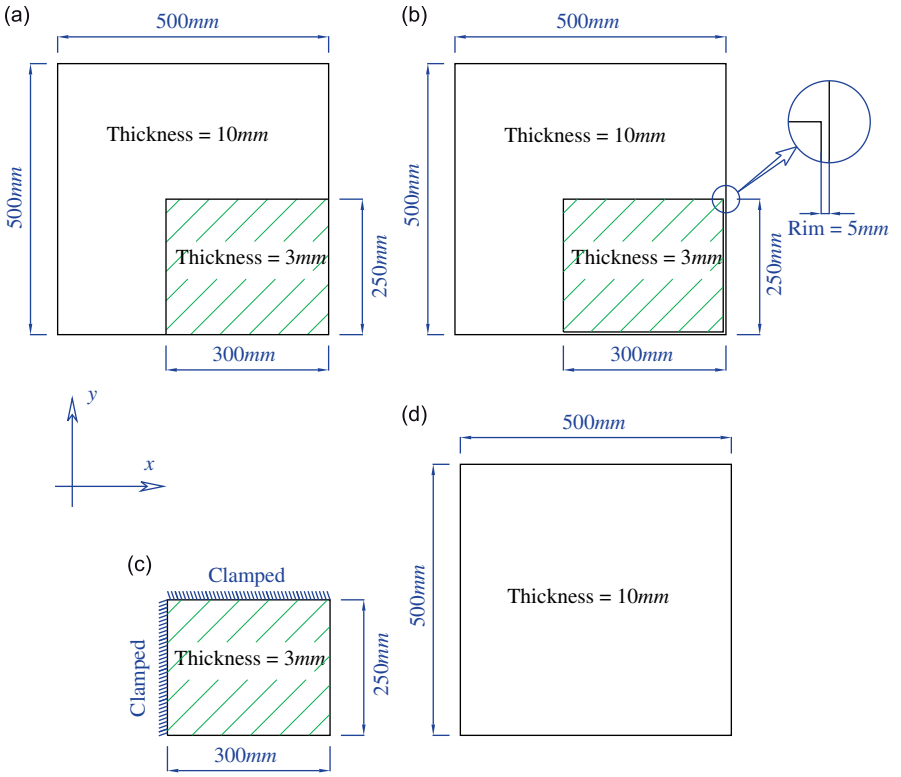

Fig. 15. Plate models with different thicknesses (a) *pC*, (b) *pCr*, (c) *pN*, (d) *pK*.

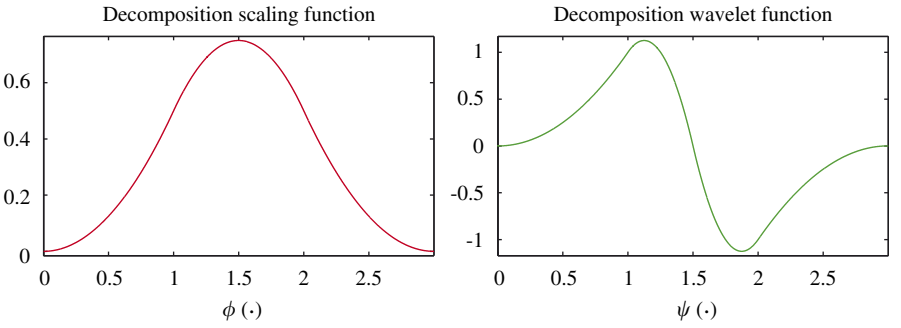

Fig. 16. Bi-orthogonal wavelet rbio3.1, scaling and wavelet functions.

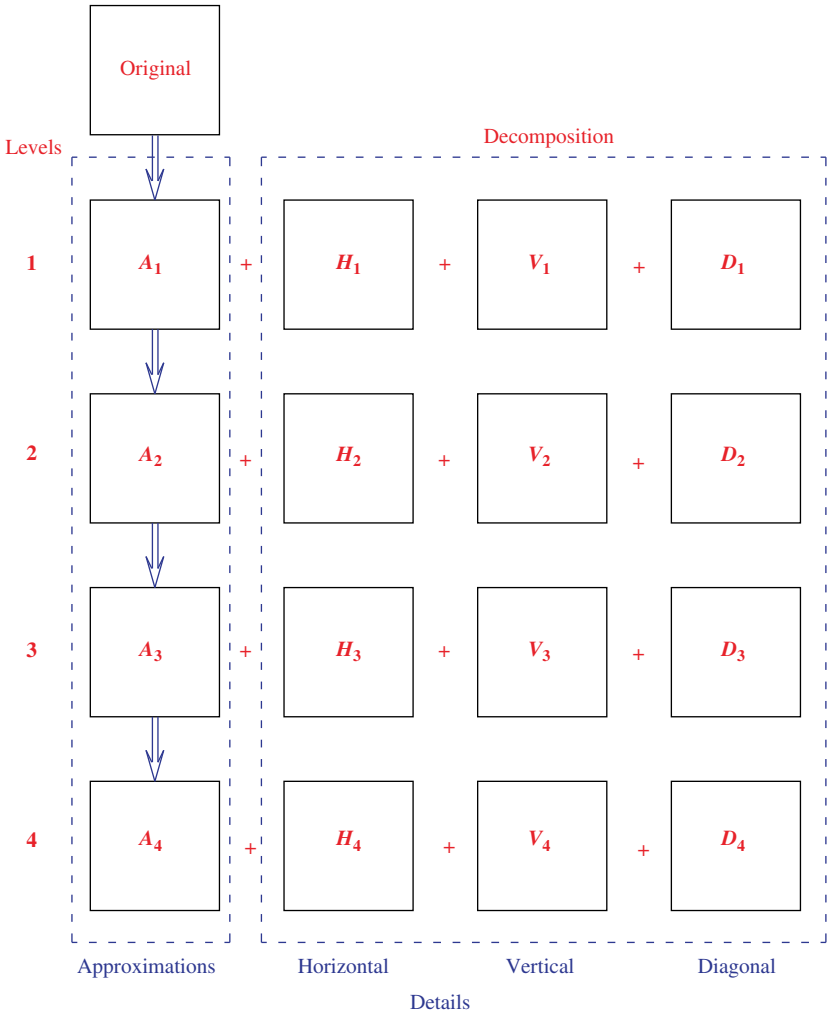

Fig. 17. Four level decomposition tree.

four diagonal detailed sub-images and 1 approximation sub-image as shown in Fig. 17. The average energy of every sub-image was calculated by Eq. (31) to form a shape feature vector.

4.3.1. Comparing pC and pN

Hierarchical clustering of the SFV formed by the energies of the 12 detailed sub-images in Fig. 17 was carried out on the plates *pC* and *pN*. The resulting dendrogram is shown in Fig. 18. A number of clusters with small distances indicate the similarity of the mode-shape details. For instance, cluster ***a*** formed by mode 2 of *pN* (N02) and mode 4 of *pC* (C04) suggests the shape of *pC* in the thin region may be similar to the shape of *pN*, which is true by visual comparison between these two modes as shown in Fig. 19(a). The correlation of the shapes between C04 and N02 on the thin region is 97.7 percent. Similar results for the clusters ***b***, ***c***, ***e*** and ***f*** may be obtained. Two more pairs of mode-shape patterns for cluster ***b*** and ***c*** shown in Fig. 19(b) and (c) have 95.7 percent and 95.8 percent correlation for the paired thin regions, respectively. Thus, the patterns in the thin regions of *pC* match the corresponding patterns of *pN* sufficiently. In addition, cluster ***d*** groups modes 11 and 12 of *pC* together. This implies that shapes from different modes of the same structure may have similar patterns in the thin region. Fig. 19(d) shows the shapes of mode 11 and the flipped version of mode 12 (flipped with respect to the axis 2–4). It can be seen that the lower-right corners of both images match well (93.1 percent). Thus it is seen that the local shapes in the thin region of the plate may be recognised from the SFV formed by the energies from the detailed sub-images.

4.3.2. Comparing pC and pCr with pK

In this section, global shape patterns of plate *pC* and *pCr* are compared with the plate having uniform thickness *pK*. The MAC of *pC* and *pK* shown in Fig. 20 indicates almost no similarity between them. It is observed that certain mode shapes in the thick region of *pC* are similar to the relative region of *pK*. In order to reveal the similarity between the modes of *pC* and

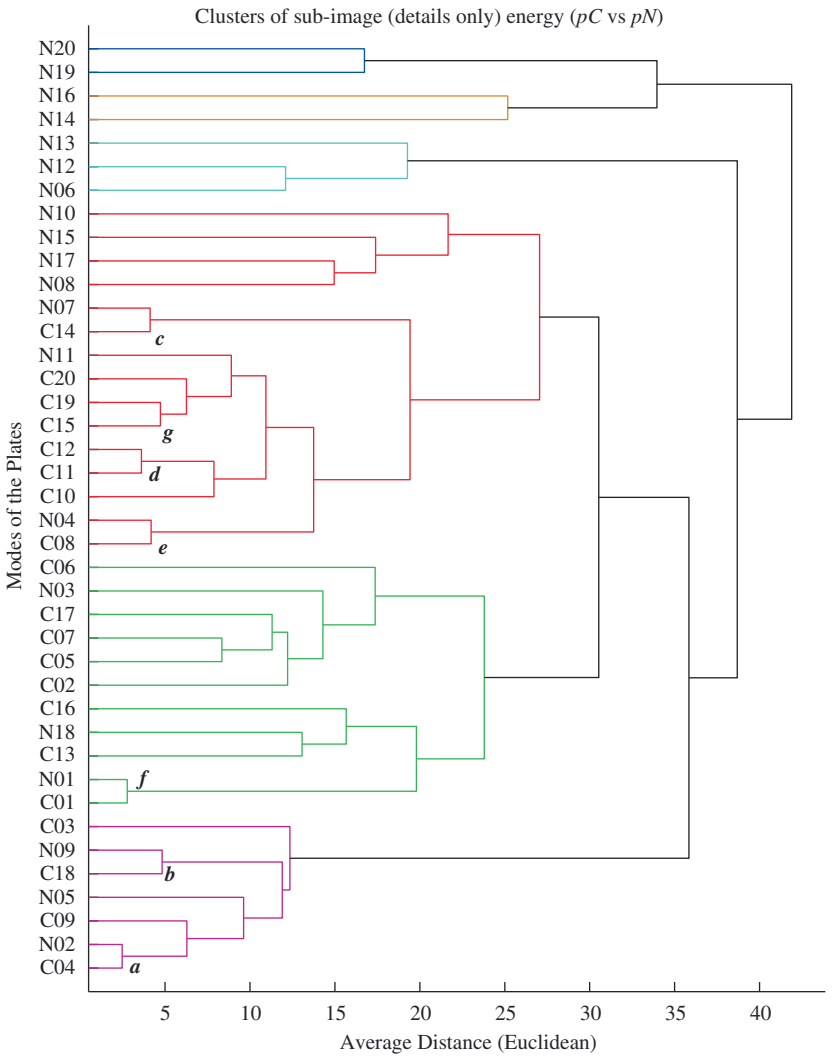

Fig. 18. Dendrogram of *pC* and *pN* by energies of detailed sub-images.

pK globally, the approximation at level 4 (A_4) of the mode shapes by the DWT2 is adopted. The analysing wavelet is the *rbio3.1*. The 2D correlation coefficients [33] for mode pairs *pC* and *pK* with correlations greater than 0.65 at approximation level 4, are shown in Fig. 21 for the approximations at levels 1–4. As described in Fig. 17, more details are removed from the approximation when the decomposition level increases. Thus, the correlation coefficients of the mode pairs increase with the decomposition levels as shown in Fig. 21. A number of well correlated pairs can be found from Fig. 21(d). For instance, 73.7 percent correlation of A_4 between mode 8 of *pC* (C_8) and mode 8 of *pK* (K_8) indicates that their global shape patterns are similar. As shown in Fig. 22(a), the pattern of the bottom-right region of *pC* is same as the 'shrunken' version of *pK*. For the pairs of C_{12}–K_6 and C_{20}–K_{12} shown in Fig. 22(b) and (c), the patterns of *pC* on the thick region are similar to those of *pK* in the corresponding region which are revealed by the 68.1 percent and 78.4 percent correlation of the global approximations A_4, respectively. If the pattern of C_5 is rotated through 90° with respect to *z*-axis, it almost perfectly matches the pattern of K_4 with a correlation of 90.6% at approximation K_4 while the correlation is 66.8% for this pair of mode shapes without any rotation as shown in Fig. 22(d).

When the two edges of the thin region of *pC* are stiffened by rims as in Fig. 15(b), it is found that the mode shapes of the stiffened plate *pCr* are more similar to *pK* than *pC*. Fig. 23 shows the threshold correlation (greater than 0.7 at level 4) of approximation at levels 1–4 between *pCr* and *pK*. It is clear that the number of high-correlation pairs between *pCr* and *pK* is greater than those between *pC* and *pK* in Fig. 21. The global dynamic characteristics of the stiffened plate *pCr* are closer to *pK* than *pC*. Similarly to Fig. 21, certain higher mode pairs become more correlated with increasing approximation level (and consequent removal of detail) as shown in Fig. 23. The four pairs of patterns, shown in Fig. 24, have high correlation coefficients at level A_4 between *pCr* and *pK* in Fig. 23(d). It can be seen that the lower-right corners of *pCr* in Fig. 24(a), (b) and (c) are the 'shrunken' version of those from *pK*, whilst the patterns on the thick region of *pCr* are extremely similar to

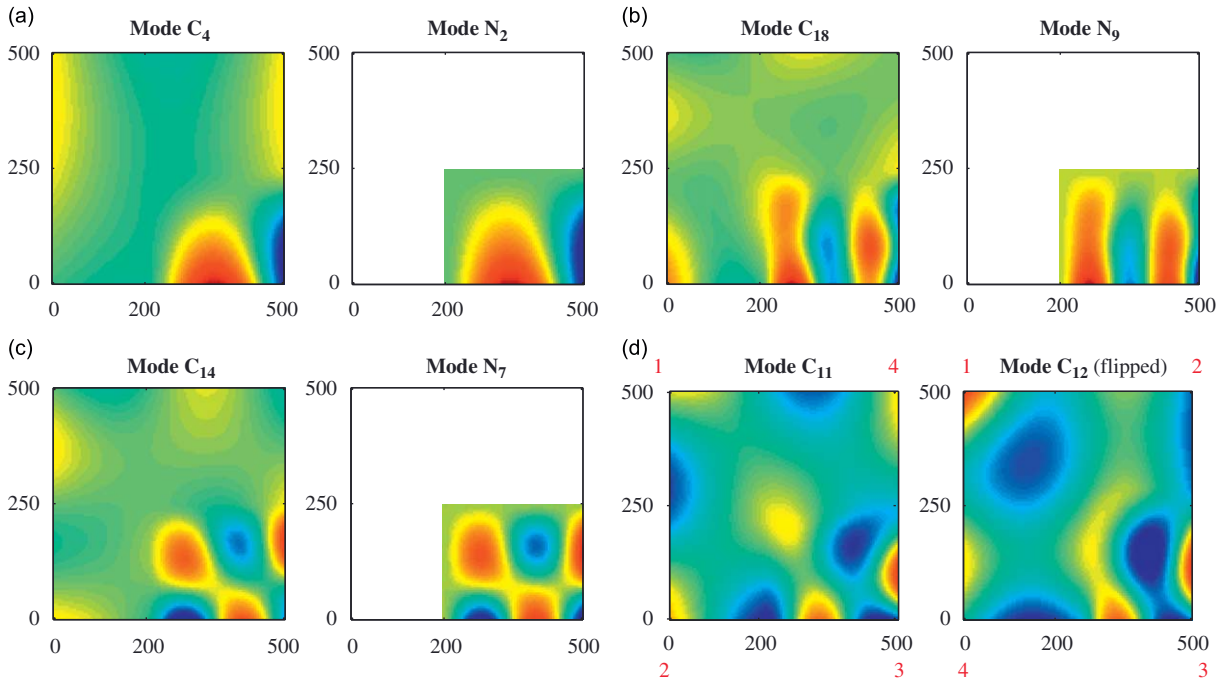

Fig. 19. Similar shape patterns in the thin region of the plate.

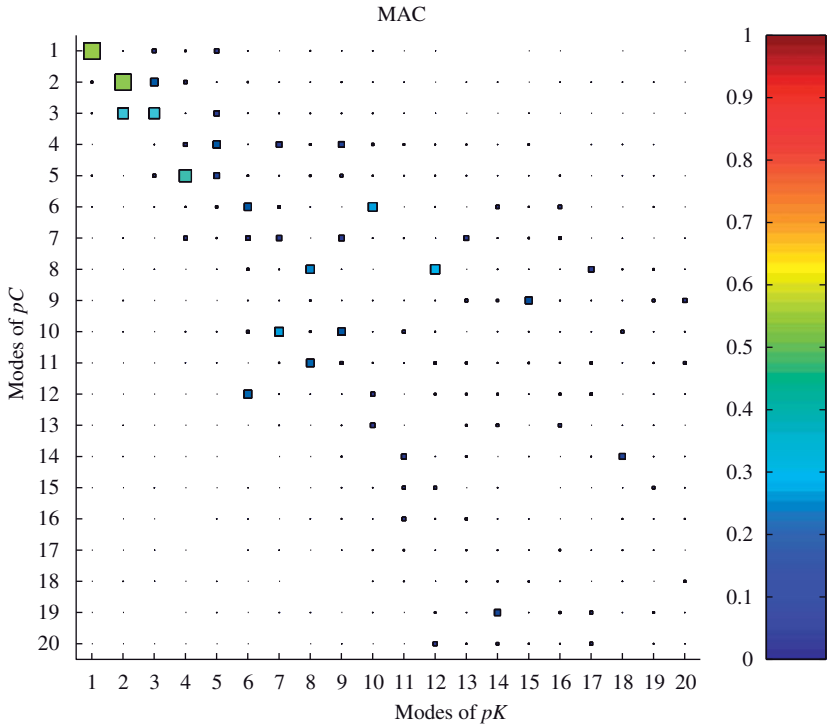

Fig. 20. MAC between pC and pK.

pK. Their correlation coefficients of A_4 are 81.6 percent, 81.9 percent and 84.9 percent, respectively. In additional, the pair shown in Fig. 24(d) having 78.4 percent correlation for A_4 is dissimilar to each other only in the thin region.

Therefore, it can be concluded from the two examples above that the WD not only detects the local shape features from the whole structure accurately, but also extracts the overall, or global, shape features.

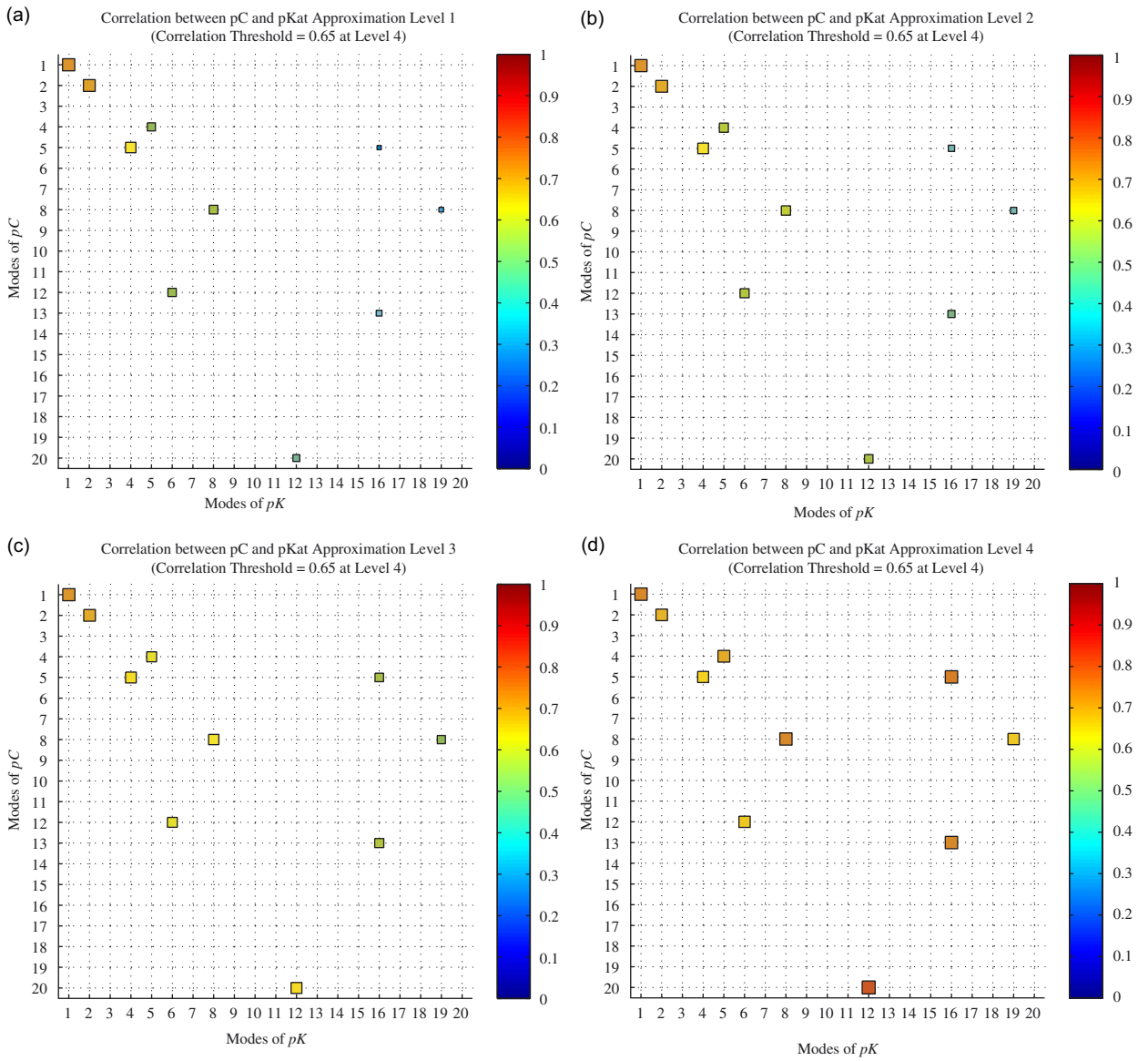

Fig. 21. Threshold correlation coefficients (greater than 0.65 at level 4) of the approximation at levels 1–4 between *pC* and *pK*: (a) level 1; (b) level 2; (c) level 3; (d) level 4.

4.4. Uncertain boundary conditions of a beam

4.4.1. Uncertain position of a sliding joint

As shown in Fig. 25, a beam with a pin joint at the left end and a sliding joint near the right end was modelled. The position of the sliding joint is assumed to be uncertain. There are 11 samples taken uniformly from the uncertain position of the joint (900 mm to 920 mm, mean value: 910 mm, standard deviation: 6.63 mm). The first nine normal modes are calculated.

Since the mode shapes of the beam can be considered as 1D spatial signals the 1D Fourier descriptor of each mode shape is used. The SFV, $\mathbf{f}_{FD}$, is constructed by the sub-band energies of the FDs with non-negative spatial frequency components. In particular, the DC component and the seven sub-band energies sorted by spatial frequency from low to high were taken into consideration for this case. So that $\mathbf{f}_{FD}$ is an 8-dimensional random variable due to the position uncertainty. Fig. 26 shows the scatter-plot matrix of the SFV $\mathbf{f}_{FD}$. Each sub-figure shows the pairwise scatter-plot of the ith vs jth ($i,j = 0,1,\ldots,7$) coordinates of $\mathbf{f}_{FD}$. It is clear that nine clusters are shown in each of the sub-figures. Every cluster has 11 points. The legends of the different modes are illustrated in the enlarged sub-figure (3rd vs 4th) as shown in Fig. 26. Also, it can be seen that the clusters of individual modes are separable in certain dimensions. For instance, the clusters of mode 1 having the largest DC

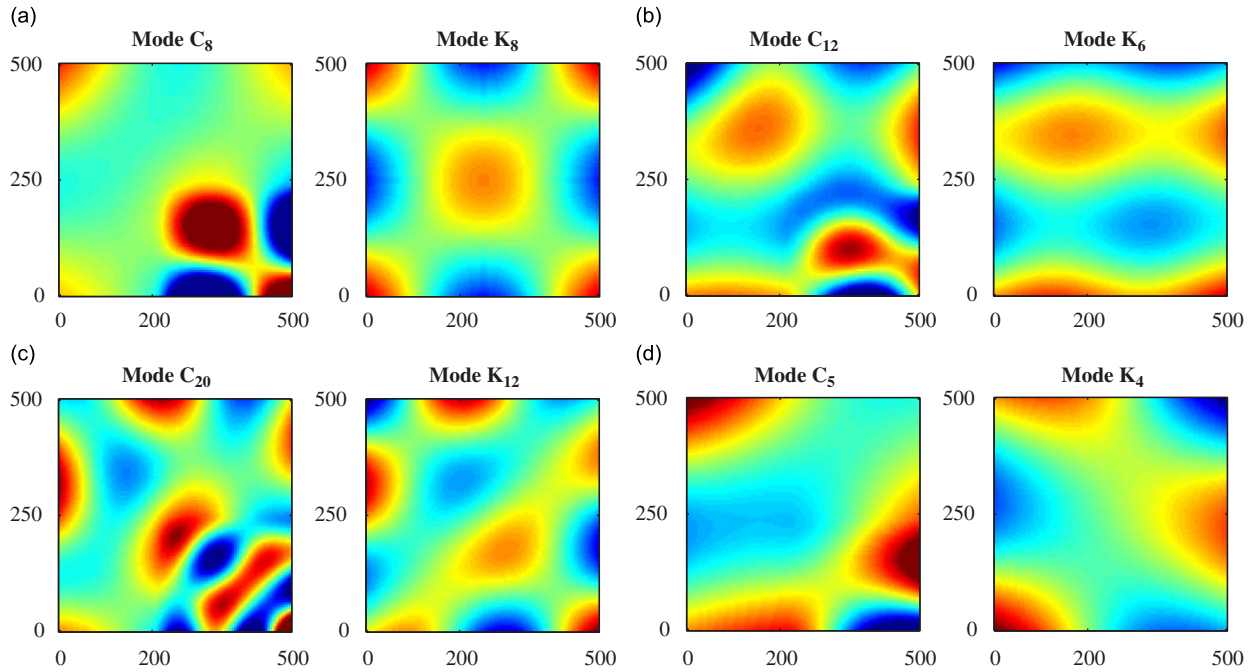

Fig. 22. Similar pairs of global shapes between *pC* and *pK*.

component are far away from the rest in the 0th column sub-figures of Fig. 26; the clusters of mode 2 in the 1st column sub-figures dominating by the 1st sub-band energy are well separated from the rest of the clusters. Similar isolated clusters of modes 3 and 4 can be found in the 2nd column sub-figures; modes 5 and 6 in the 3rd column; mode 7 in the 4th column; modes 8 and 9 in the 5th column.

Similarity measurement of the mode shapes based on the SFV $\mathbf{f}_{\mathrm{FD}}$ is carried out by a hierarchical clustering algorithm and shown in Fig. 27. The digits (1–9) on the vertical axis denote the modes and the upper-case letters (A to K) denote the different sample positions of the sliding joint. It can be seen that the SFVs of the same mode are grouped closely together. However, when two modes are considered that are in different groups it is seen that they are far away from each other. Thus, the SFV $\mathbf{f}_{\mathrm{FD}}$ constructed from the FDs shows the desirable property of modal separation. It presents small intra-class (within the same mode clusters) distances and large inter-class (between two mode clusters) distances.

As most of the clusters having elongated characteristics as shown in Fig. 26, principal component analysis (PCA) is applied to reduce the dimensionality of the feature vector. A brief discussion of PCA may be found in Appendix A. Taking mode 3 for example, the 11 feature vectors are projected onto the principal component space by

$$\mathbf{S}_3 = \mathbf{P}_3\mathbf{F}_3 \tag{35}$$

where

$$\mathbf{F}_3 = [\mathbf{f}_{FD}^{3,1} - \boldsymbol{\mu}_{FD}^{3}, \ldots, \mathbf{f}_{FD}^{3,i} - \boldsymbol{\mu}_{FD}^{3}, \ldots \mathbf{f}_{FD}^{3,11} - \boldsymbol{\mu}_{FD}^{3}] \tag{36}$$

is the 8×11 (dimensionality $\times$ samples) centred feature matrix of the mode 3 with $\mathbf{f}_{FD}^{3,i}$ represents the SFV of the ith sample and $\boldsymbol{\mu}_{FD}^{3}$ is the vector of mean values. $\mathbf{P}_3$ is the 8×8 orthonormal matrix with rows which are the principal vectors of $\mathbf{F}_3$; that is the eigenvectors of the covariance matrix of $\mathbf{F}_3$ sorted in the order of decreasing component variance (the eigenvalue of the covariance matrix). $\mathbf{S}_3$ is the projection of $\mathbf{F}_3$ in the principal component space $\mathbf{P}_3$. Thus, $\mathbf{S_3}$ a diagonal covariance matrix. Table 1 shows the eight component variances of mode 3 in decreasing order. It is clear that the 1st component variance dominates the total variance and the other seven variances are negligible. This means that the 11 SFVs of mode 3 are distributed mainly in the direction of the 1st principal component, which is the 1st row of the matrix $\mathbf{P}_3$. So that retaining only the 1st row of the matrix $\mathbf{S}_3$ is sufficient to represent the cluster of mode 3. Therefore, the dimensionality of the SFV may now be reduced from 8×1 to 1×1.

The first five principal component variances of every individual cluster of the 9 modes are listed in Table 2 by percentage. All modes can be almost completely described by the 1st principal component (the first PC variances of all the nine modes are greater than 98 percent as shown in the second row of Table 2), which may be interpreted as the $\mathbf{f}_{FD}$ of these modes being distributed linearly in the shape feature space. Thus, these linear clusters, considered as line segments in a hyperplane, can be represented by the coefficients of their 1st principal components and their mean values as

$$\mathscr{C}_k = t_k\mathbf{p}_1^k + \boldsymbol{\mu}_{FD}^k, \quad t_k \in [t_{k,1}, t_{k,2}], \quad k = 1, 2, \ldots, 9 \tag{37}$$

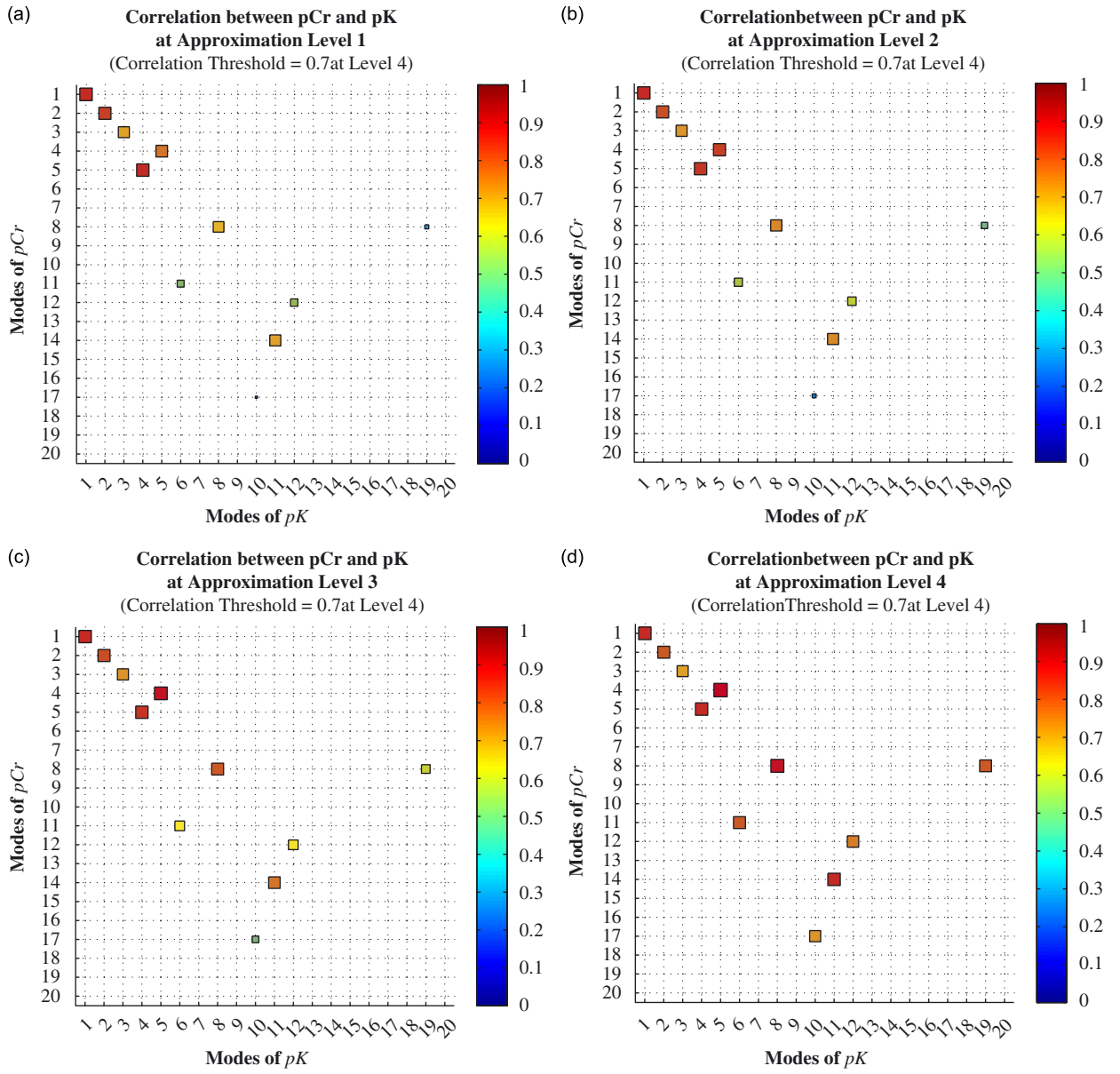

Fig. 23. Threshold correlation coefficients (greater than 0.7 at level 4) of the approximation at levels 1–4 between *pCr* and *pK*: (a) level 1; (b) level 2.

where the superscript/subscript k represents the kth mode; t_k having the values between $[t_{k,1},t_{k,2}]$ is the scaling parameters; $\mathbf{p}_1^k$ is the 1st principal component and $\boldsymbol{\mu}_{FD}^k$ is the mean value of the feature vector $\mathbf{f}_{FD}$ from all samples.

For any new SFV $\mathbf{f}_{FD}^{test}$ needing to be compared to the nine clusters, projection onto the 1st principal component $\mathbf{p}_1^k$ of the nine modes should be carried out first,

$$s_1^k = (\mathbf{f}_{FD}^{test} - \boldsymbol{\mu}_{FD}^k) \cdot (\mathbf{p}_1^k)^{\mathrm{T}} \tag{38}$$

Since the characteristics of the nine clusters indicated by the PCA are almost linear, the distance between $\mathbf{f}_{FD}^{test}$ and any mode (cluster), as illustrated in Fig. 28, can be defined by

$$\mathscr{d}_k^p(\mathbf{f}_{FD}^{test}, \mathscr{C}_k) = \sqrt{||\mathbf{f}_{FD}^{test} - \boldsymbol{\mu}_{FD}^k||^2 - (s_1^k)^2} \tag{39}$$

where $||\cdot||$ denotes the norm of the vector. Therefore, the SFV $\mathbf{f}_{FD}^{test}$ is assigned to the mode k if $\mathscr{d}_k^p$ is the minimum out of all the modes. For instance, another new sample of the sliding joint position (at 922 mm—slightly outside the uncertain range assumed above) is taken. Feature vectors of the first nine modes are considered. The point-to-line distance of each mode of

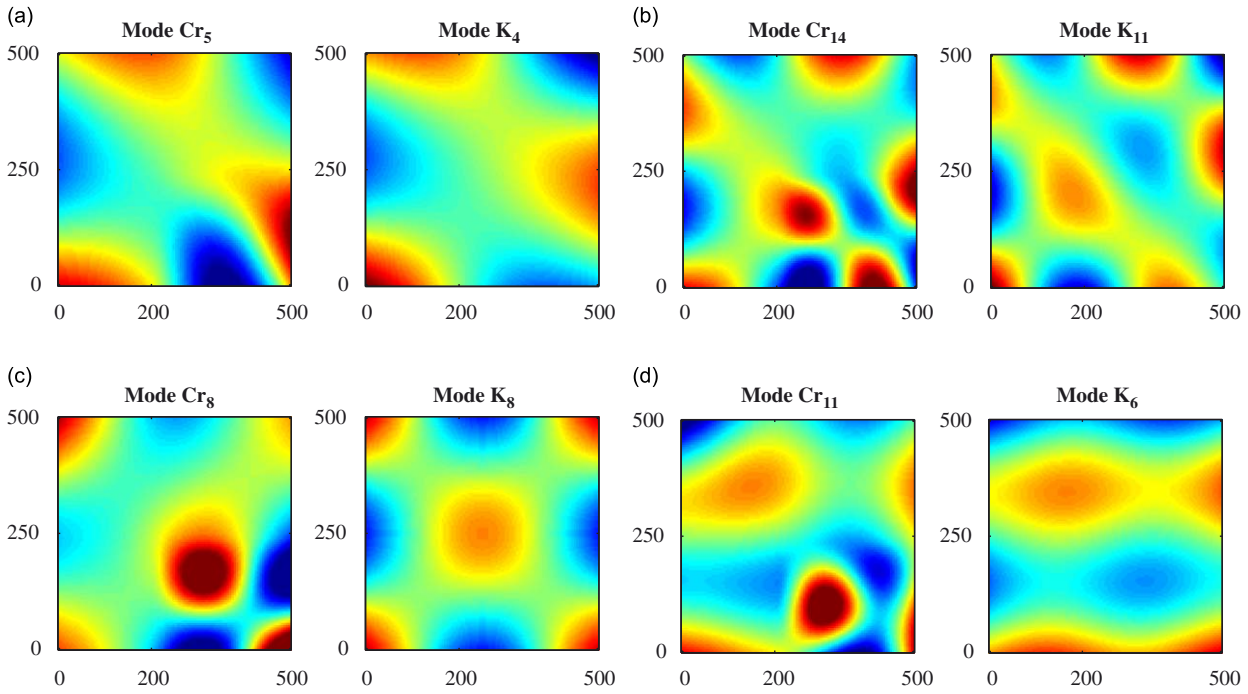

Fig. 24. Similar pairs of global shapes—*pCr* and *pK*.

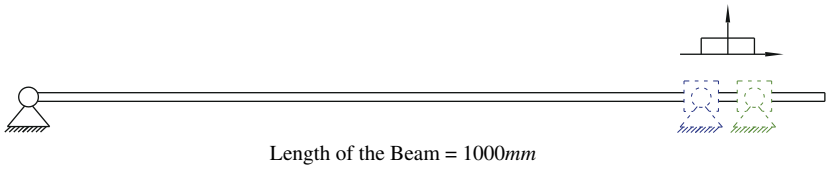

Fig. 25. Finite-element beam model with uncertain position of the sliding joint.

the test sample to the nine statistical clusters based on the Fourier SFV are calculated and shown in Table 3. It is clear the minimum distances indicate that every single mode of the $\mathbf{f}_{FD}^{test}$ falls into the statistical cluster describing the same mode because the minimum value in each row of Table 3 lies on the diagonal and is far smaller than the other values.

Thus, the degree of similarity of the test SFV can initially be determined by finding the minimum point-to-line distance, $\min(d_k^p)$, for each of the nine clusters. However, d_k^p is only the perpendicular distance to the principal direction of the linear cluster. A further distance measurement, the Mahalanobis distance, along the direction of the linear cluster should also be taken into consideration to ensure that the test SFV falls into the corresponding cluster.

The Mahalanobis distance d_k^M takes into account the correlation of the data and is independent of scale. The Mahalanobis distance between the test SFV and the mean value of the cluster along the direction of the 1st principal component is written as

$$d_k^M(\mathbf{f}_{FD}^{test}, \mathscr{C}_k) = \frac{s_1^k}{\sigma_1^k} \tag{40}$$

where σ_1^k is the standard deviation of the clusters at the direction of the 1st principal component. It is seen that $d_k^M < 1$ when the projection of the test SFV onto the direction of the 1st principal component is less than the standard deviation and $d_k^M > 1$ when greater. Hence, the Mahalanobis distance of the test SFV to the cluster as indicated by the minimum d_k^p should be close to unity because it is supposed to fall in the cluster. If the cluster of the test SFV assigned by $\min(d_k^p)$ has very large Mahalanobis distance, e.g. $d_k^M \gg 1$, the assignment of the test SFV needs to be reconsidered by assigning it to the cluster with the second minimum d_k^p and rechecking the corresponding Mahalanobis distance.

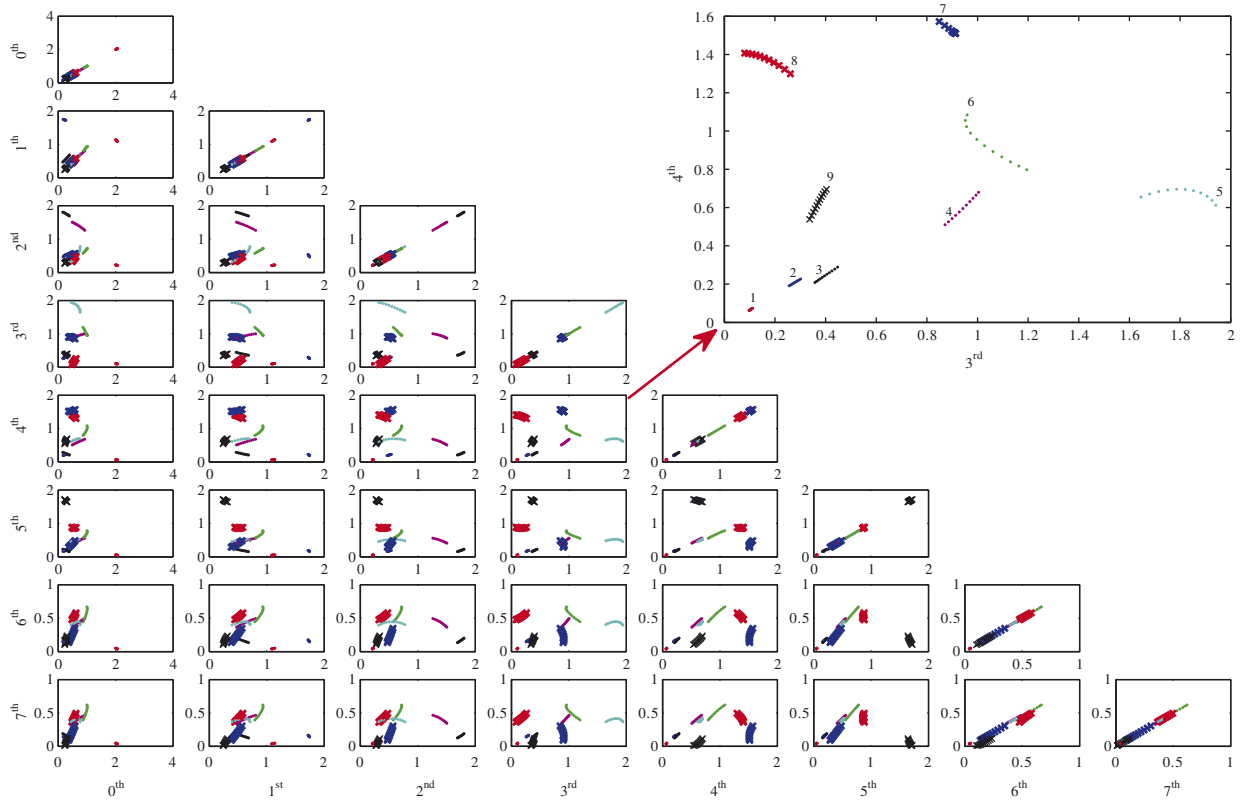

Fig. 26. Scatter plot of the 8-dimensional SFV (the ordinal number represents the sub-band energies).

Table 4 lists the d_k^M of the nine modes of the test SFVs to their corresponding statistical clusters as indicated in Table 3. Their average value of d_k^M, $k = 1,2,\ldots,9$ in Table 4 indicates that the SFV of the test sample is generally 1.828 times the standard deviation from the mean, and might therefore be considered to reasonably belong to the cluster. It corresponds to the sliding joint position of this sample because the Mahalanobis distance of the test sample to the mean position is

$$d_{joint}^M = \frac{(922 - 910\,\text{mm})}{6.63\,\text{mm}} = 1.8091 \tag{41}$$

which is approximately equal to the average of the Mahalanobis distance of its SFVs.

The mode shapes of the beam with uncertain joint positions can be represented by the FD effectively because each mode shape is described by an 8×1 Fourier SFV $\mathbf{f}_{FD}$. The similarities between different mode shapes are measured by a hierarchical clustering algorithm with average distance criterion based on $\mathbf{f}_{FD}$ as shown in Fig. 27. The statistical characteristics of different modes of the Fourier SFV are extracted and described by the PCA. Recognition of a test sample based on $\mathbf{f}_{FD}$ can be carried out efficiently and accurately by the point-to-line and the Mahalanobis distances.

4.4.2. *Uncertain spring stiffnesses*

Another bending beam model having a pin joint at the left end and two springs, one translational k_y and one rotational k_w, attached to the right end is shown in Fig. 29. The stiffness of the two springs, assumed to be uncertain, obey a bivariate Gaussian distribution. Ten-thousand random samples were generated with the mean values ($\mu_{ky} = 10 \times 10^5$, $\mu_{kw} = 1.5 \times 10^3$) and 20 percent standard deviations ($\sigma_{k_y} = 2 \times 10^5$, $\sigma_{k_w} = 3 \times 10^2$) as shown in Fig. 30. The first six modes were calculated. Bending energy, as defined Appendix C, was adopted as a general shape descriptor for these mode shapes. Thus, the feature vector $\mathbf{f}_{BE}$ was a scalar. The class-conditional probability density of the bending energy of each mode was estimated by the Parzen window method (described in Appendix B) based on 10 000 stiffness samples. The univariate Gaussian kernel is adopted in this case. Fig. 31 shows the estimated probability densities of the six modes.

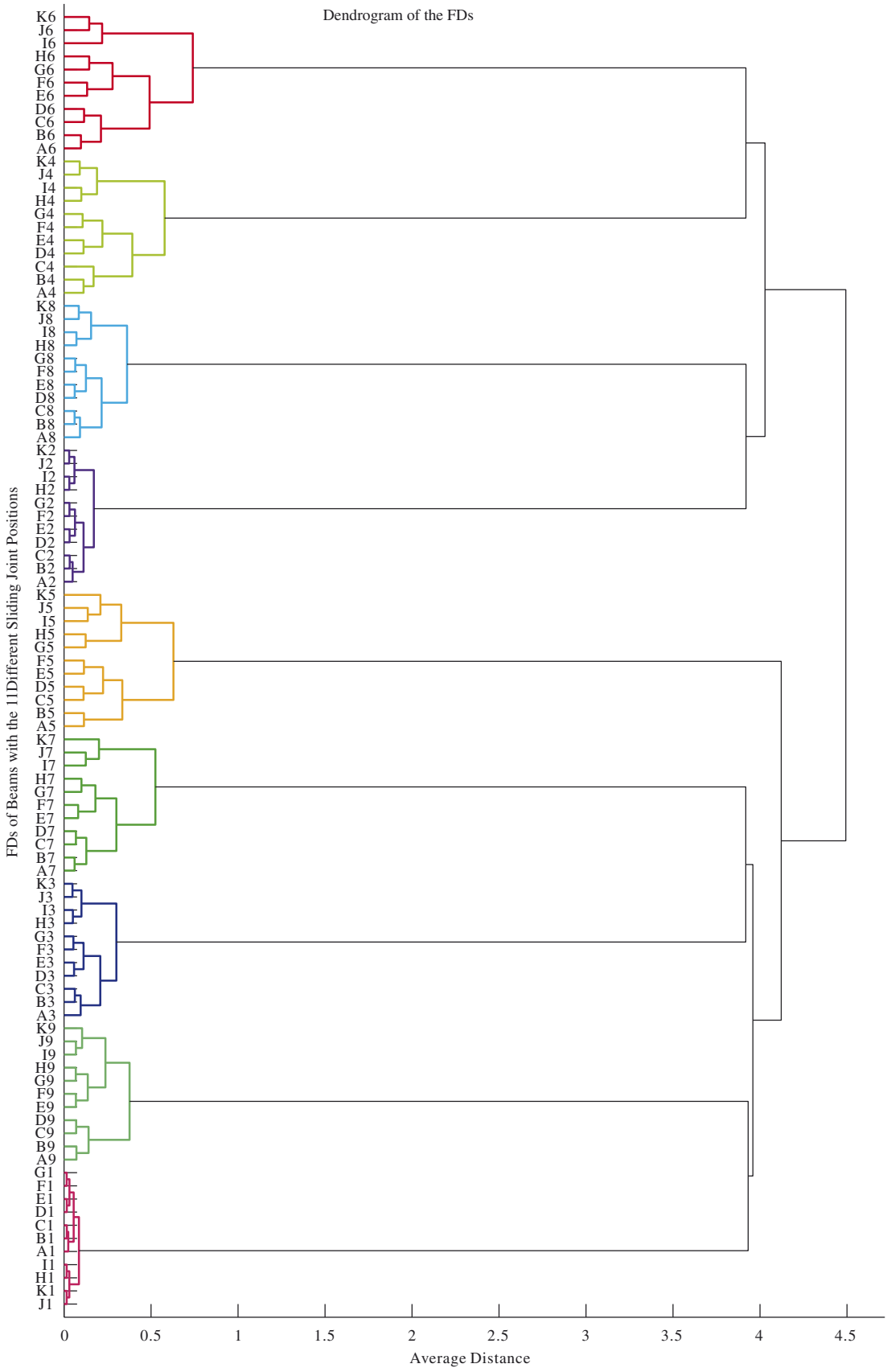

Fig. 27. Dendrogram of the FDs.

Table 1
Eigenvalues of covariance matrix of $\mathbf{F}_3$ in decreasing order.

	1st	2nd	3rd	4th	5th	6th	7th	8th
Component variance	1.57×10^{-2}	1.13×10^{-5}	5.01×10^{-5}	4.85×10^{-11}	1.28×10^{-13}	0.00	0.00	0.00
Percentage	99.93	0.07	0.00	0.00	0.00	0.00	0.00	0.00

Table 2
The percentage of the total variance explained by each principal component.

Mode	1	2	3	4	5	6	7	8	9
PC—variance									
1st	**99.97**%	**99.88**%	**99.23**%	**98.26**%	**98.00**%	**98.89**%	**99.04**%	**99.31**%	**99.53**%
2nd	0.03%	0.12%	0.77%	1.74%	1.96%	1.08%	0.95%	0.68%	0.46%
3rd	0.00%	0.00%	0.00%	0.00%	0.04%	0.02%	0.01%	0.01%	0.00%
4th	0.00%	0.00%	0.00%	0.00%	0.00%	0.00%	0.00%	0.00%	0.00%
5th	0.00%	0.00%	0.00%	0.00%	0.00%	0.00%	0.00%	0.00%	0.00%

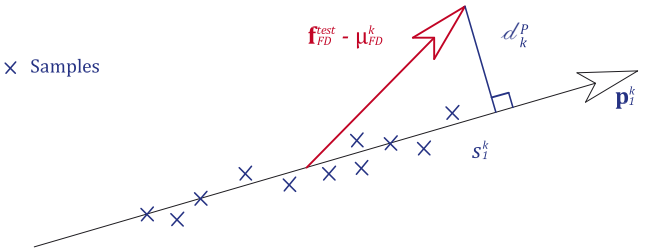

Fig. 28. Distance of a point from a line.

Table 3
Point to line distance.

	Modes of the test SFV								
	1	2	3	4	5	6	7	8	9
Modes of the clusters									
1	**0.0005**	1.7375	1.3461	2.0050	2.1168	1.9656	2.3831	2.1949	2.5449
2	0.8474	**0.0023**	1.4034	1.8195	1.9513	1.7002	1.9941	1.8740	2.1002
3	1.8856	1.2811	**0.0085**	0.7302	1.5822	1.6591	1.8747	1.8002	2.0457
4	2.0605	1.2807	0.6739	**0.0216**	1.1171	1.1812	1.4355	1.3785	1.6253
5	2.4605	2.0295	2.2006	1.5486	**0.1340**	0.7335	1.4448	1.8165	1.821
6	1.7614	1.0886	1.8729	0.6060	0.8356	**0.0971**	0.5654	0.3953	0.7682
7	2.0804	1.5907	1.9130	1.2311	1.2720	0.8850	**0.0518**	0.7563	0.9733
8	1.9416	1.523	1.8829	1.3039	1.5636	0.8893	0.7215	**0.0399**	0.6026
9	2.3365	1.9686	2.0803	1.7475	1.8741	1.5564	1.5730	1.1501	**0.0251**

Table 4
The Mahalanobis distance between the test SFV and the mean of the clusters.

Mode	1	2	3	4	5	6	7	8	9	Average	STD
d_k^M	1.760	1.729	1.659	1.644	1.971	1.346	2.197	2.232	1.918	**1.828**	**0.282**

To test any SFV $\mathbf{f}_{BE}^{test}$ that needs to be assigned to one of the modes, the Bayesian decision rule is applied to determine the minimum risk of the test SFV. Substituting $\mathbf{f}_{BE}^{test}$ into Eq. (56) (given in Appendix B) leads to

$$R(c_i|\mathbf{f}_{BE}^{test}) = \sum_{j=1}^{k} \lambda(c_i, c_j) p(c_j|\mathbf{f}_{BE}^{test}) \tag{42}$$

Also, the *zero-one* loss function is assumed for this case, i.e.

$$\lambda(c_i, c_j) = \begin{cases} 0 & i = j \\ 1 & i \neq j \end{cases} \quad i,j = 1,2,\ldots k \tag{43}$$

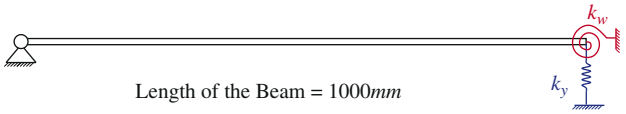

Fig. 29. Finite element of beam with uncertain spring stiffnesses of k_y and k_w.

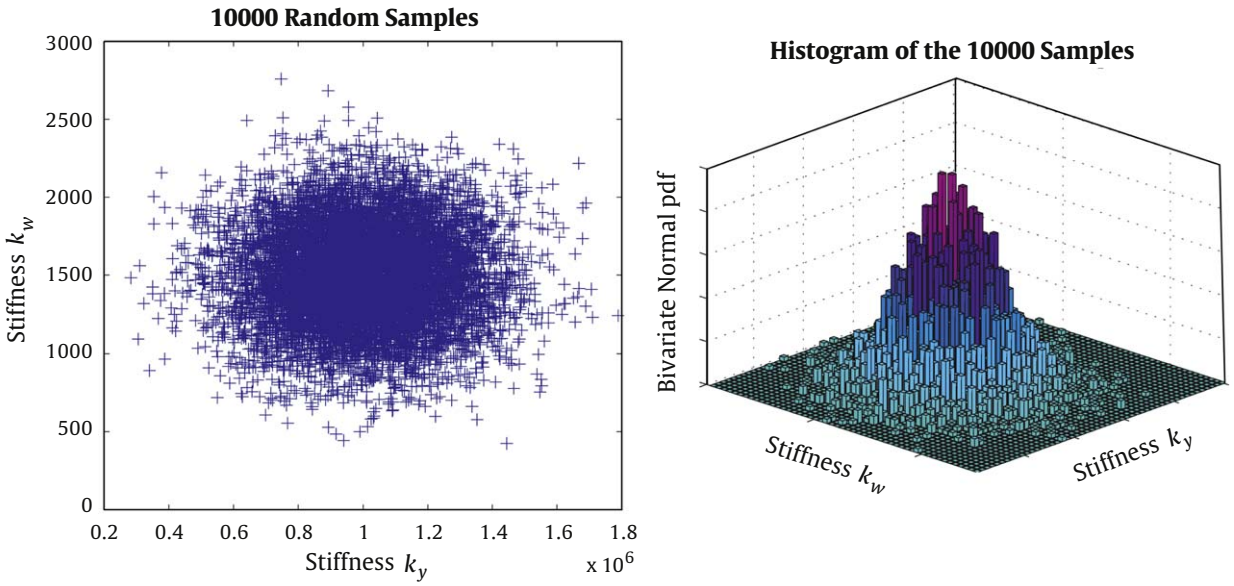

Fig. 30. Random samples from bivariate Gaussian distribution (by Marsaglia's Ziggurat algorithm).

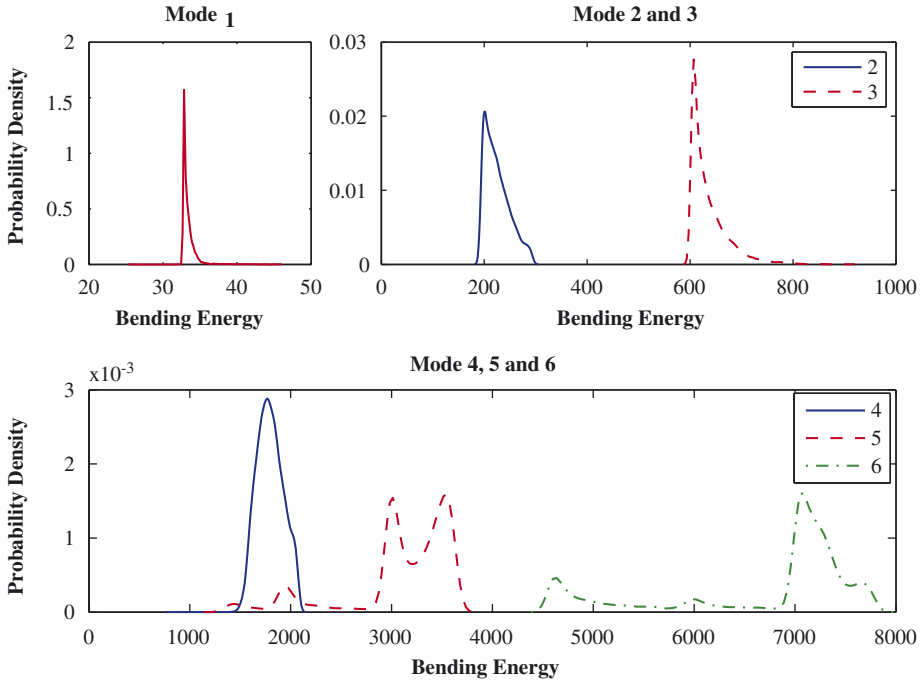

Fig. 31. Probability density of bending energies fitted by the Parzen window method (normal kernel function).

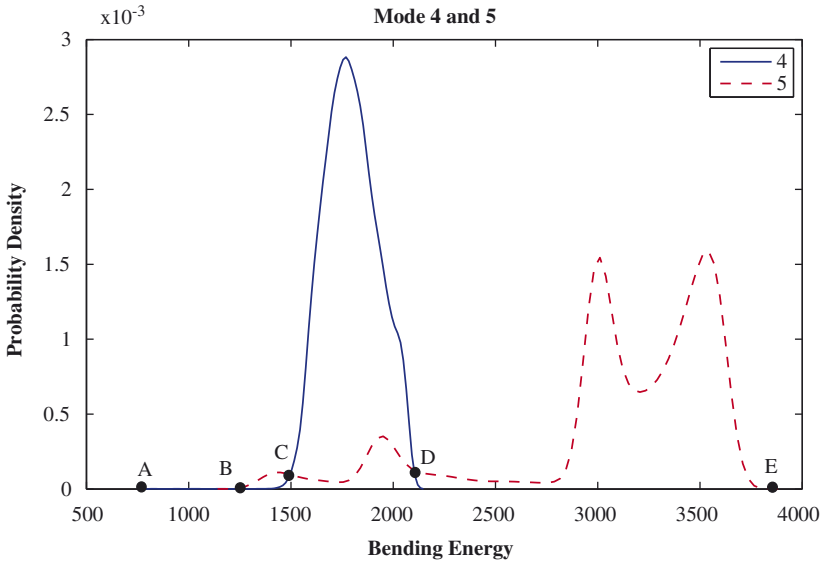

Fig. 32. Overlapped probability densities of modes 4 and 5.

meaning that no loss will be allocated to a correct decision and a unity loss to a wrong decision. Therefore, Eq. (42) can be written as

$$R(c_i|\mathbf{f}_{BE}^{test}) = \sum_{i\neq j} P(c_j|\mathbf{f}_{BE}^{test}) = 1 - P(c_j|\mathbf{f}_{BE}^{test}) \tag{44}$$

which represents the average probability of misclassification. Thus, the Bayesian decision rule can be simplified as maximising the *posterior* probability $P(c_j|\mathbf{f}_{BE}^{test})$, also called the maximum *a-posterior* (MAP) rule, in Eq. (44). Then the test pattern $\mathbf{f}_{BE}^{test}$ is assigned to class c_i if

$$P(c_i|\mathbf{f}_{BE}^{test}) > P(c_j|\mathbf{f}_{BE}^{test}) \quad \forall i \neq j \tag{45}$$

Applying the Bayes formula (Eq. (54)) on (45) yields,

$$\frac{\mathscr{P}(\mathbf{f}_{BE}^{test}|c_i)P(c_i)}{\mathscr{P}(\mathbf{f}_{BE}^{test})} > \frac{\mathscr{P}(\mathbf{f}_{BE}^{test}|c_j)P(c_j)}{\mathscr{P}(\mathbf{f}_{BE}^{test})} \quad \forall i \neq j \tag{46}$$

which can be re-written as

$$\mathscr{P}(\mathbf{f}_{BE}^{test}|c_i)P(c_i) = \max_{j=1,\ldots,k}\{\mathscr{P}(\mathbf{f}_{BE}^{test}|c_j)P(c_j)\} \tag{47}$$

Furthermore, the *prior* probabilities $P(c_j)_{j=1,2,\ldots,6}$, the probability of being of mode j, are the same and equal to $\frac{1}{6}$. Thus, Eq. (47) can be simplified as

$$\mathscr{P}(\mathbf{f}_{BE}^{test}|c_i) = \max_{j=1,\ldots,k}\{\mathscr{P}(\mathbf{f}_{BE}^{test}|c_j)\} \tag{48}$$

indicating that the assignment of the pattern $\mathbf{f}_{BE}^{test}$ depends only on its maximum class-conditional density function.

It is apparent from Fig. 31 that the conditional density for mode 1, 2, 3 and 6 are well-separated from each other. Any pattern $\mathbf{f}_{BE}^{test}$ in these regions can easily be assigned to the corresponding modes. However, a portion of conditional density of mode 5 overlaps with the conditional density of mode 4. An enlarged version of these two densities is shown in Fig. 32. If the test pattern falling with the region (C, D), mode 4 is assigned as $\mathscr{P}(\mathbf{f}_{BE}^{test}|c_4) > P(\mathbf{f}_{BE}^{test}|c_5)$. Mode 5 will be returned if $\mathbf{f}_{BE}^{test}$ is in either of the regions (B, C) or (D, E). Mode 4 is returned when $\mathbf{f}_{BE}^{test}$ is between (A, B).

5. Conclusions

The conventional method for comparing mode shapes, the MAC correlation, results in a single numerical value to assess the similarity between mode-shape vectors. Further information on the subtle difference in shape of two modes may be obtained by using image processing methods that have been used to good effect in other areas of science and engineering

as well as in medicine and forensics. New techniques for vibration mode shape recognition using image processing and pattern recognition are presented. A variety of shape descriptors with the capability of recognising mode-shape differences are described. The SDs show the desirable properties of computational efficiency and ease of image reconstruction using a small number of SD terms. Different advantages of various shape descriptors are determined by their individual properties. Specifically, the ZMD is powerful in discriminating circular and spherical mode shapes; the FD is more general and very effective at extracting mode-shape features by virtue of its sinusoidal kernel; the WD shows the capability of distinguishing between local and global features. Deterministic and stochastic pattern classification techniques such as correlation, hierarchical clustering, Euclidian and the Mahalanobis distances, principal component analysis and Bayesian decision theory are examined to compare and classify the shape feature vectors assembled from different shape descriptors. The choice of the shape descriptor and classification method depends on the structure in hand.

Though the mode shape recognition involves a set of methods, the procedure is determinate. The problem of mode-shape comparison is transformed into the classification of the shape feature vectors assembled from different shape descriptors. The present study provides a series of alternative approaches with different advantages and offering a more complete understanding of modes shapes to complement the conventional MAC correlation.

Acknowledgements

The first author wishes to acknowledge the support of an Overseas Research Studentship (ORS), a University of Liverpool Studentship, an award from the University of Liverpool Graduate Association (Hong Kong) and EC project ADVISE (Advanced Dynamic Validations using Integrated Simulation and Experimentation) Grant 218595.

Appendix A. Principal component analysis (PCA)

The PCA, also known as the Karhunen–Loève transform, performs an orthogonal linear transformation on the feature vectors such that the transformed feature vectors are uncorrelated with each other in the new coordinate system. The covariance matrix of the transformed feature vectors is diagonal with the terms arranged in descending order. The first diagonal terms with greatest variance is followed next on the diagonal by the second greatest variance and so on.

This transform can be expressed as

$$\mathbf{S} = \mathbf{PF} \tag{49}$$

where $\mathbf{F}$ is the $l \times N$ (feature dimensionality $\times$ total samples) centred feature matrix, having zero empirical mean, constructed by

$$\mathbf{F} = [\mathbf{f}_1 - \boldsymbol{\mu}, \ldots, \mathbf{f}_i - \boldsymbol{\mu}, \ldots, \mathbf{f}_N - \boldsymbol{\mu}] \tag{50}$$

with $\mathbf{f}_1$ is the ith SFV from the N samples and $\boldsymbol{\mu}$ is the mean. $\mathbf{P}$ is the orthonormal transformation basis and $\mathbf{S}$ is the projection $\mathbf{F}$ onto $\mathbf{P}$ expressed as

$$\mathbf{S} = [\mathbf{s}_1, \ldots, \mathbf{s}_i, \ldots, \mathbf{s}_N] \tag{51}$$

Since the objective of this linear transform is to make the matrix $\mathbf{S}$ having diagonal covariance matrix, the matrix $\mathbf{P}$ can be constructed by the eigenvectors of the covariance matrix of $\mathbf{F}$ [34]. These eigenvectors are called principal components of $\mathbf{F}$ and sorted in descending order by their corresponding eigenvalues (component variance). Thus,

$$\mathbf{P} = \begin{bmatrix} \mathbf{p}_1 \\ \mathbf{p}_2 \\ \vdots \\ \mathbf{p}_l \end{bmatrix} \tag{52}$$

where $\mathbf{p}_1$, a $1 \times l$; row vector, is the 1st principal component having the greatest component variance; $\mathbf{p}_2$ is the 2nd principal component with second greatest component variance and so on. The least significant eigenvector $\mathbf{p}_l$ has the smallest component variance.

Hence, the dimensionality of feature vectors can now be reduced by keeping those coordinates of the transformed feature vectors that contribute most to the total variance. i.e. retaining the first m principal components and rewriting Eq. (49) as,

$$[\tilde{\mathbf{s}}_1, \ldots, \tilde{\mathbf{s}}_i, \ldots, \tilde{\mathbf{s}}_N] \equiv \tilde{\mathrm{S}} = \tilde{\mathbf{P}}\mathbf{F} = \begin{bmatrix} \mathbf{p}_1 \\ \mathbf{p}_2 \\ \vdots \\ \mathbf{p}_m \end{bmatrix} \mathbf{F}, \quad m \ll l \tag{53}$$

where $\tilde{\mathbf{s}}_i$, $i = 1, 2, \ldots, N$ are the dimensionality reduced SFVs.

Appendix B. Bayesian decision rules

Let $\{c_1,c_2,\ldots c_k\}$ denote the finite set of k classes (modes) of patterns (mode-shapes) based on the feature vectors $\mathbf{f}=(f_1,f_2,\ldots f_1)^{\mathrm{T}}$ which are assumed to have a probability density function conditioned on the pattern class. For any pattern $\mathbf{f}$ belonging to class c_j can be considered as an observation drawn randomly from the class-conditional probability function $\mathscr{P}(\mathbf{f}|c_j)$. $P(c_j)$ describes the *prior* probability of an individual being of the class c_j. Thus the *posterior* probability $P(c_j|\mathbf{f})$ can be calculated from $\mathscr{P}(\mathbf{f}|c_j)$ by the Bayes formula:

$$P(c_j|\mathbf{f})=\frac{\mathscr{P}(\mathbf{f}|c_j)P(c_j)}{\mathscr{P}(\mathbf{f})} \tag{54}$$

where the *evidence* $\mathscr{P}(\mathbf{f})$ is

$$\mathscr{P}(\mathbf{f})=\sum_{j=1}^{k}\mathscr{P}(\mathbf{f}|c_j)P(c_j) \tag{55}$$

Then the *Bayesian decision rule* may be stated as assigning a pattern $\mathbf{f}$ to class c_j if the conditional risk

$$R(c_i|\mathbf{f})=\sum_{j=1}^{k}\lambda(c_i,c_j)P(c_j|\mathbf{f}) \tag{56}$$

is a minimum, where $\lambda(c_i,c_j)$, known as the loss function, is the loss incurred in deciding to take class c_i when the true class is c_j.

B.1. Parzen window

In real applications that the *prior* probabilities are easy to obtain but the class-conditional probability density functions are difficult to estimate in parametric forms. The Parzen window method [35] provides a non-parametric technique for such estimates. The probability density function can be estimated by

$$\hat{\mathscr{P}}(\mathbf{f})=\frac{1}{h^l}\left(\frac{1}{N}\sum_{i=1}^{N}\tau\left(\frac{\mathbf{f}-\mathbf{f}_i}{h}\right)\right) \tag{57}$$

where $\mathbf{f}_i$, $i=1,2,\ldots,N$ represent the SFVs of the N samples, $\tau(\cdot)$ is the Parzen window (or *kernel function*) such that

$$\tau(\mathbf{u})\geq 0 \quad \text{and} \quad \int_{\mathrm{u}}\tau(\mathbf{u})\mathrm{d}\mathbf{u}=1 \tag{58}$$

h is the width of $\tau(\mathbf{u})$ in one dimension and h^l is the volume of the l-dimensional hyper-cubic. One of the common choices for the Parzen window is the multidimensional Gaussian function written as

$$\tau_G(\mathbf{u})=\frac{1}{(2\pi h)^{l/2}|\mathbf{\Sigma}|^{1/2}}\exp\left\{-\frac{1}{2h^2}(\mathbf{u}-\mathbf{u}_i)^{\mathrm{T}}\mathbf{\Sigma}^{-1}(\mathbf{u}-\mathbf{u}_i)\right\} \tag{59}$$

Appendix C. Curvature and bending energy

Suppose $\gamma(t)=\{x(t),y(t)\}$ is the parametric representation of a 2D curve. The curvature $\mathscr{K}(t)$ of $\gamma(t)$ is defined as [36],

$$\mathscr{K}(t)=\frac{\dot{x}(t)\ddot{y}(t)-\ddot{x}(t)\dot{y}(t)}{(\dot{x}(t)^2+\dot{y}(t)^2)^{3/2}} \tag{60}$$

where t, the parameter of the variables x and y, is commonly defined as the normalised curve length by

$$t=\frac{s}{L},\quad t\in[0,1] \tag{61}$$

where s denotes a position measured along the curve and L is the total length.

The bending energy of a 2D curve can be defined as:

$$\mathscr{D}_{BE}=\frac{1}{L}\int_{Curve}\mathscr{K}(t)^2\,\mathrm{d}t \tag{62}$$

References

[1] M.I. Friswell, J.E. Mottershead, *Finite Element Model Updating in Structural Dynamics*, Kluwer Academic Publishers, Dordrecht, 1995.
[2] R.J. Allemang, D.L. Brown, A correlation coefficient for modal vector analysis, *Proceedings of First International Modal Analysis Conference*, Vol. 1, 1982, pp. 110–116.
[3] A.B. Stanbridge, D.J. Ewins, Modal testing using a scanning laser Doppler vibrometer, *Mechanical Systems and Signal Processing* 13 (1999) 255–270.
[4] A.B. Stanbridge, M. Martarelli, D.J. Ewins, Measuring area vibration mode shapes with a continuous-scan LDV, *Measurement* 35 (2004) 181–189.
[5] T.C. Chu, W.F. Ranson, M.A. Sutton, W.H. Peters, Applications of digital-image-correlation techniques to experimental mechanics, *Experimental Mechanics* 25 (1985) 232–244.
[6] N. Perez de la Blanca-Garrido, Physically-based active shape models: initialisation and optimisation, *Pattern Recognition* 31 (1998) 1003–1017.
[7] A.K. Jain, R.P.W. Duin, J. Mao, Statistical pattern recognition: a review, *IEEE Transactions on Pattern Analysis and Machine Intelligence* 22 (2000) 4–37.
[8] L. da Fontooura Costa, Roberto Marcondes Cesar Jr., *Shape Analysis and Classification Theory and Practice*, CRC Press, Boca Raton, 2001.
[9] D. Zhang, G. Lu, Review of shape representation and description techniques, *Pattern Recognition* 37 (2004) 19.
[10] S. Loncaric, A survey of shape analysis techniques, *Pattern Recognition* 31 (1998) 983–1001.
[11] M.K. Hu, Visual pattern recognition by moment invariants, *IRE Transactions on Information Theory* IT-8 (1962) 179–187.
[12] M.R. Teague, Image analysis via the general theory of moments, *Optical Society of America* 70 (1980) 920–930.
[13] C.H. Teh, R.T. Chin, On image analysis by the methods of moments, *IEEE Transactions on Pattern Analysis and Machine Intelligence* 10 (1988) 496–513.
[14] R.J. Prokop, A.P. Reeves, A survey of moment-based techniques for unoccluded object representation and recognition, *Graphical Models Image Processing* 54 (1992) 438–460.
[15] A. Khotanzad, Y.H. Hong, Invariant image recognition by zernike moments, *IEEE Transactions on Pattern Analysis and Machine Intelligence* 12 (1990) 489–498.
[16] R.L. Cosgriff, Identification of shape, Report no. 820-11, Ohio State University Research Foundation, 1960.
[17] C.T. Zahn, R.Z. Roskies, Fourier descriptors for plane closed curves, *IEEE Transactions on Computers* C21 (1972) 269–281.
[18] G.H. Granlund, Fourier preprocessing for hand print character recognition, *IEEE Transactions on Computers* C-21 (2) (1972) 195–201.
[19] E. Persoon, K.-S. Fu, Shape discrimination using Fourier descriptors, *IEEE Transactions on Systems, Man and Cybernetics* SMC-7 (1977) 170–179.
[20] G. Eichmann, Shape representation by Gabor expansion, *Hybrid Image and Signal Processing II, SPIE* 1279 (1990) 86–94.
[21] S.G. Mallat, A theory for multiresolution signal decomposition: the wavelet representation, *IEEE Transactions on Pattern Analysis and Machine Intelligence* 11 (1989) 674–693.
[22] G.C.-H. Chuang, C.-C. Jay Kuo, Wavelet descriptor of planar curves: theory and applications, *IEEE Transactions on Image Processing* 5 (1996) 56–70.
[23] L. Devroye, L. Gyorfi, G. Lugosi, *A Probabilistic Theory of Pattern Recognition*, Springer, Berlin, 1996.
[24] G.J. McLachlan, *Discriminant Analysis and Statistical Pattern Recognition*, Wiley-Interscience, New York, 2004.
[25] A.K. Jain, N.N. Murty, P.J. Flynn, Data clustering: a review, *ACM Computing Surveys* 31 (1999) 264–323.
[26] F. Zernike, Translated: diffraction theory of the cut procedure and its improved form, the phase contrast method, *Physica* 1 (1934).
[27] P. Hew, *Orthogonal functions on the unit disk having invariance in form*, The University of Western Australia, 1996.
[28] I. Daubechies, *Ten Lectures on Wavelets*, Society for Industrial and Applied Mathematics, 1992.
[29] I. Daubechies, Orthonormal bases of compactly supported wavelets, *Communications on Pure and Applied Mathematics* 41 (1988) 909–996.
[30] R.O. Duda, P. Hart, D. Stork, *Pattern Classification and Scene Analysis*, Wiley, New York, 2001.
[31] T.P. Ryan, *Modern Engineering Statistics*, Wiley-Interscience, New York, 2007.
[32] W. Wang, J.E. Mottershead, C. Mares, Mode-shape recognition and finite element model updating using the Zernike moment descriptor, *Mechanical Systems and Signal Processing* 2009 〈http://dx.doi.org/10.1016/j.ymssp.2009.03.015〉.
[33] J.A. Rice, *Mathematical Statistics and Data Analysis*, Duxbury Press, 2007.
[34] B.S. Everitt, G. Dunn, *Applied Multivariate Data Analysis*, 2nd ed., Arnold, London, 2001.
[35] E. Parzen, On estimation of a probability density function and mode, *The Annals of Mathematical Statistics* 33 (1962) 1065–1076.
[36] I. Young, J. Walker, J. Bowie, An analysis technique for biological shape I, *Information Control* 25 (1974) 357–370.